POLITECNICO DI TORINO

Master's Degree in Aerospace Engineering

Master's Degree Thesis

Plasma-based swirling jets

Supervisors

Prof. Jacopo SERPIERI

Prof. Gioacchino CAFIERO

Candidate

Manuel ZANNONE

October 2024

Abstract

Jet flows characterized by the superposition of an azimuthal velocity component on a conventional round jet are defined as swirling jets. The induction of rotational motion to a free flow generated with a round nozzle enhances heat transfer and flame stabilization capability, making these jets widely used in industrial applications. The swirling motion is usually achieved by passive methods such as guided vanes (helical inserts) or rotating perforated plates.

The aim of this study was to validate the feasibility of generating and controlling swirling jets without the use of moving parts or internal inserts. Four pairs of Dielectric Barrier Discharge plasma actuators (DBD-PAs) were instead positioned along the axial direction of the injector and evenly distributed around its circumference, so that the body force exerted by them would impart a circumferential velocity component to the axisymmetric jet flow, allowing the swirl number to be adjusted without any drag penalty and providing the capability of active control. The jet facility at the Politecnico di Torino aerospace department's laboratory Modesto Panetti was reconfigured with a new nozzle (specifically designed and 3D-printed) and a seeding system. The former made it possible to easily change the setup configuration in order to evaluate different cases, while the latter allowed the measurement campaign to be carried out using the Stereoscopic Particle Image Velocimetry technique.

The effects induced by the active swirl generators were compared with those of the 3D-printed passive swirl generator by acquiring the flow field at several x/D distances from the nozzle exit section. The swirl numbers obtained using DBD-PAs were found to be lower than those obtained using guided vanes, this being attributed to the dielectric material which did not allow the employment of higher voltages. The study successfully validated the potential of this active control design, identifying areas for future enhancement. A novel actuation approach, consisting in the sequential triggering of the DBD-PAs, was also tested and validated.

Table of Contents

List of Tables

List of Figures

Chapter 1

Introduction

1.1 Swirling jets

Swirling jets are one kind of jet flows characterized by an azimuthal velocity component superimposed on a conventional round jet. This particular flows are employed in various applications among which it is possible to mention the field of combustion. Indeed, one of their peculiar characteristics is their ability to improve the combustion efficiency by enhancing the flame stabilization.

Swirling jets are obtained by inducing a rotational motion to a free flow generated with a round nozzle, resulting in an increase in the spread, width, growth, decay, entrainment, turbulence level of the jet and an enhancement of the mixing with the surrounding fluid [1].

The swirling motion generates radial and axial pressure gradients which can have a strong influence on the flow field. In fact, in the presence of a strong swirl it is possible to observe a reverse flow along the axis due to the high adverse axial pressure gradient [2].

1.1.1 Characteristics

A swirling jet can be identified by three main characteristics:

- the flow rate
- the rotation rate
- the swirl generation method

The method by which the swirl is generated plays a crucial role in the evolution of swirling flows, as it determines the initial velocity distribution, which varies depending on the specific generation method employed [3].

To quantify the flow rate and rotation rate, two non-dimensional parameters can be used: the *Reynolds number* (*Re*) and the *Swirl number* (*S*), respectively.
The *Reynolds number* can be defined as reported in [4]:

$$Re = \frac{2R\overline{V_x}(x_0)}{\nu} \tag{1.1}$$

where $\overline{V_x}(x_0)$ is the mean axial velocity at the nozzle exit, R is the radius of the orifice and ν is the kinematic viscosity.

With regard to the swirl number, there is no single formulation, but as noted in [1], this dimensionless parameter is in various forms either the velocity or momentum ratio of the azimuthal to axial velocity components.
One definition of the swirl number as the momentum ratio can be found in [2],[5], [6] and [7]:

$$S = \frac{G_\theta}{G_x R} \tag{1.2}$$

where G_θ is the axial flux of azimuthal momentum and G_x is the axial flux of axial momentum and can be defined as follows:

$$G_\theta = 2\pi\rho \int_0^R r^2 \left(uw + \overline{u'w'} \right) dr \tag{1.3}$$

$$G_x = 2\pi\rho \int_0^R r \left(u^2 - \tfrac{1}{2}w^2 + \overline{u'^2} - \tfrac{1}{2}\left(\overline{w'^2} + \overline{v'^2} \right) \right) dr \tag{1.4}$$

In these equations (1.2, 1.3 and 1.4), R is the radius of the nozzle, ρ is the density of the fluid, r is the radial coordinate, u, v and w are the axial, radial and tangential components of the velocity vector respectively, whereas u', v' and w' are their turbulent fluctuations. From the above literature it can be seen that the *Reynolds stress component* $\overline{u'w'}$ and the quantity $[\overline{u'^2} - \frac{1}{2}\left(\overline{w'^2} + \overline{v'^2}\right)]$ are conventionally neglected as they are assumed to be smaller than the mean velocity terms and the term u^2 respectively. Following these assumptions, it is possible to rewrite the equations 1.3 and 1.4:

$$G_\theta = 2\pi\rho \int_0^R r^2 uw \, dr \tag{1.5}$$

$$G_x = 2\pi\rho \int_0^R r \left(u^2 - \tfrac{1}{2}w^2 \right) dr \tag{1.6}$$

so the *swirl number* can be expressed by the following equation:

$$S = \frac{\int_0^R r^2 uw \, dr}{\left[\int_0^R r \left(u^2 - \frac{1}{2}w^2 \right) dr \right] \cdot R} \tag{1.7}$$

A definition of the swirl number as the ratio of azimuthal to axial velocities can be found in [4]:

$$S = \frac{2V_\theta(\frac{R}{2}, x_0)}{V_x(0, x_0)} = \frac{2w(\frac{R}{2}, x_0)}{u(0, x_0)} \tag{1.8}$$

where $2V_\theta({}^{R}\!/{}_{2}, x_0)$ is the azimuthal velocity measured at half the radius of the nozzle exit and $V_x(0, x_0)$ is the axial velocity measured on the axis of the jet. This definition has been found to be more appropriate for vortex breakdown studies, partly because it requires velocity measurements to be taken at only two locations. Four different types of jets can be defined according to the swirl number:

- $S = 0$**:** non-swirling jets
- $0 < S \leq 0.4$**:** weak swirling jets
- $0.4 < S \leq 0.6$**:** moderate swirling jets
- $S > 0.6$**:** strong swirling jets

Velocity profile

As stated before, swirling jets are strongly dependant on the method used to generate the swirl as this can affect the initial velocity distribution. From Figure 1.1 it is possible to observe the radial distributions of the axial velocity component for a generic free swirling flow and its different shapes depending on the swirl number. As described in [2] and [6], for weak and moderate degrees of swirl the jet expands similarly to a single jet and the velocity profile has a Gaussian shape. Conversely, at higher swirl levels, the maximum velocity is displaced from the jet axis.

An interesting visualization of the evolution of the velocity profile along the jet axis for a swirling jet generated by an annular nozzle is shown in Figure 1.2.

In [6], a faster decay of the maximum values of the axial, tangential and radial velocity components along the length of the jets is reported for increasing degrees of swirl; more specifically, the axial and radial velocity components decay as x^{-1} and the tangential component decays as x^{-2}.

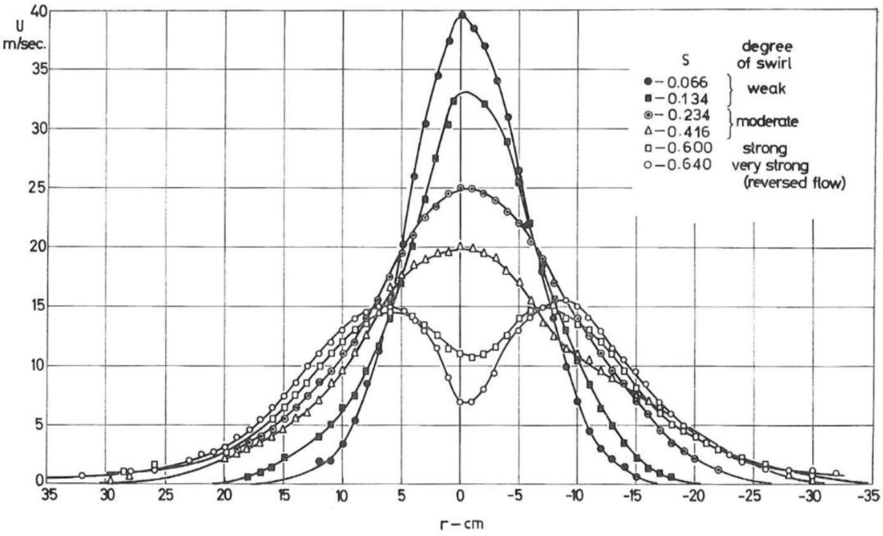

Figure 1.1: Radial distributions of axial velocity component measured at $\frac{x}{D} = 4.1$ from the nozzle exit (reproduced from [2]).

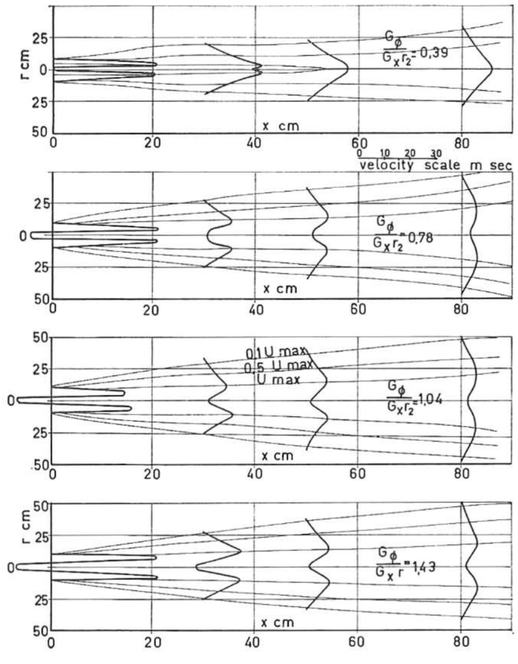

Figure 1.2: Profiles of axial-velocity component for varying degrees of swirl (reproduced from [6]).

Swirling impinging jets

High heat transfer and radial uniformity are some of the most sought-after characteristics for various applications, such as electronic cooling, which can be achieved through the use of swirling impinging jets. As noted in [8], swirling impinging jets differ from circular impinging jets in the tangential velocity components that leads to a spiral-shaped motion and in the widening of the impinged area. The radial spread causes a decrease in the axial velocity at the centre of the jet and leads to the formation of recirculation zones. A schematic representation of the flow fields of a circular impinging jet and a swirling impinging jet with their characteristic regions is shown in Figure 1.3.

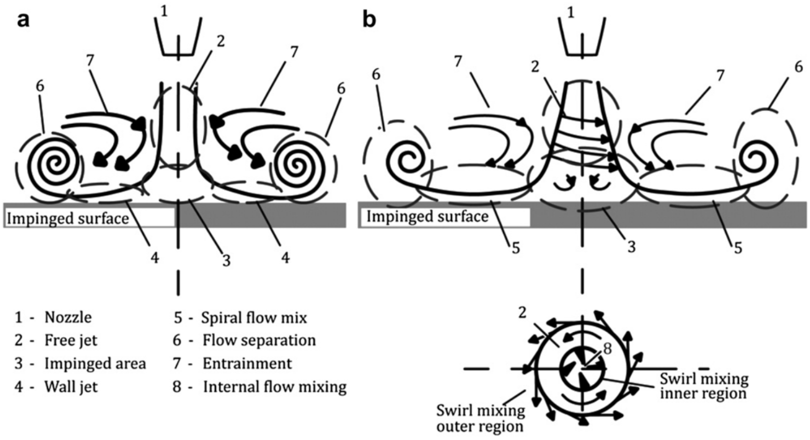

Figure 1.3: Flow topological structures of: (a) circular impinging jet, (b) swirling impinging jet (reproduced from [8]).

The heat transfer distribution is strongly dependent on the degree of swirl and, in addition, it has been observed that for small nozzle-to-plate distances, the heat transfer achieved with swirling jets is greater than that achieved with non-swirling flows, irrespective of the swirl number. Conversely, for large nozzle-to-plate distances, the effect of heat transfer enhancement is negligible.

1.1.2 Swirl generation methods

The swirling motion can be induced by a variety of methods, both with and without the capability of active control. A detailed description of the conventional methods is provided in [2], but they can be narrowed down to three main types: guided vanes, the introduction of a tangential flow into the swirl generator and the rotation of a perforated plate.

An innovative method consisting in the use of dielectric barrier discharge (DBD) plasma actuators to obtain a swirling jet was presented in [9]. Specifically, four pairs of plasma actuators were oriented along the jet axis to induce a circumferential velocity and create a swirling jet without any insertion or moving part, thus allowing the swirl number to be adjusted without any drag penalty. Because of its dielectric properties, a quartz tube was used as an injector in order to separate the electrodes (two thin copper sheets) of the DBD actuators.
As noted in [10], the plasma swirler can continuously accelerate the same fluid particles, unlike traditional spanwise-orientated actuators which can only accelerate the same fluid particles once, as these fluid particles pass through the plasma only once. After being accelerated multiple times, the fluid particles flow out of the plasma swirler with an increased azimuthal velocity. A schematic of the plasma swirler used in [9] and [10] is shown in Figure 1.4, which also depicts the flow path of the fluid particles near the plasma actuators.
An important aspect to highlight is what was found in [10] i.e. that "the swirl number increases almost linearly with the increase of the electrode length until it reaches its maximum at the end of the electrodes".

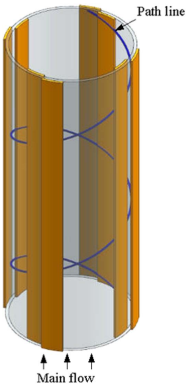

Figure 1.4: Schematic of the plasma swirler (reproduced from [10]).

Plasma swirlers with straight electrodes have the disadvantage of a non-uniform plasma distribution along the injector, which can affect the flow control effectiveness so, despite their lower power consumption, higher tangential velocity and simpler manufacturing process, a new design was presented in [11]. This new plasma swirler is shown in Figure 1.5 (a) and consists of DBD actuators with helical electrodes and, whilst mitigating the negative aspects of the previous design, can be used in conjunction with traditional mechanical swirlers. When helical shaped electrodes are employed, the central recirculation zone (CRZ) is wider compared with the one originated from the straight electrode actuation.

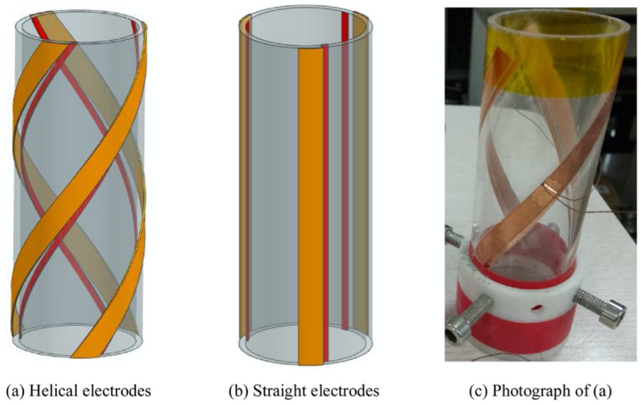

(a) Helical electrodes (b) Straight electrodes (c) Photograph of (a)

Figure 1.5: Configurations of plasma swirl injectors with electrodes of helical type and straight type (reproduced from [11]).

1.1.3 Measurement techniques

The main techniques adopted for the experimental observations of this three-dimensional flow are:

- Multi-hole pressure probe techniques
- Hot-Wire Anemometry
- Particle Image Velocimetry
- Infrared Thermography

The first two techniques are discussed in detail in [3], the PIV was used in [1], in [11] and in [12] and the IR thermography was used in [8].

Multi-hole pressure probe techniques

Multi-hole pressure probes can be used to measure static and total pressure and the magnitude and direction of the velocity vector. These probes can be found with different tip designs such as spherical, conical or pyramidal heads. The direction of flow can be determined using two different approaches: the *nulling method* and the *non-nulling method*. In the first approach, the probes are rotated in the flow field until the "direction-sensing" pressures are nulled (i.e. the probe is aligned with the flow). In the latter, the probes are fixed and the flow direction is determined using a correlation between the probe pressures and the flow direction.

A five-hole probe can be used with satisfactory results in swirling flows and angles under 20 degrees. At higher flow angles, the separation of the flow at the tip of the probe makes it challenging to obtain useful flow information because one of the side ports "becomes almost a stagnation point while the opposite port measures in the separated wake" [3]. This problem can be overcome with a specific calibration technique, but the preferable choice is to use a seven-hole probe.

Hot-Wire Anemometry

This technique can be used to obtain turbulence quantities and mean velocity components. In terms of swirling flow investigation, this can be achieved by two methods: the multi-orientation of a single hot wire and the use of a three-sensor probe.

In the first method, a single hot-wire probe is placed at several different positions, offset from each other by an angle that can vary from 30 to 45 degrees. It was concluded that this technique can provide adequate flow field measurement for any flow direction except when the flow is predominantly towards the probe holder.

The use of the three-sensor probe allows simultaneous measurement of the three components of the mean velocity and of the six components of the Reynolds stress tensor. The mean velocity measurements obtained using this method are in good agreement with those obtained using five-hole probes.

Particle Image Velocimetry

PIV is a non-intrusive optical technique and, depending on the number of velocity components to be analysed, different configurations have been used to measure the instantaneous velocity fields of swirling jets.

Planar (2D) PIV allows the evaluation of two or three velocity components (2C or 3C) in a planar section of the flow. The plane is defined by a sheet of light generated by a laser source. As they cross the plane, the seeding particles following the flow reflect the light and a camera (or set of cameras) records their position at each instant.

The 2D2C PIV measures the two velocity components contained in the plane captured by the camera; this configuration was adopted in [1] using a CCD camera, a Nd:YAG laser and olive oil droplets as seeding particles. With 2D3C PIV (stereo PIV) it is also possible to measure the third velocity component perpendicular to the plane.

This configuration has been widely used in the literature on swirling jets; Figure 1.6 shows some experimental setups adopted to study these flows. In [11], a

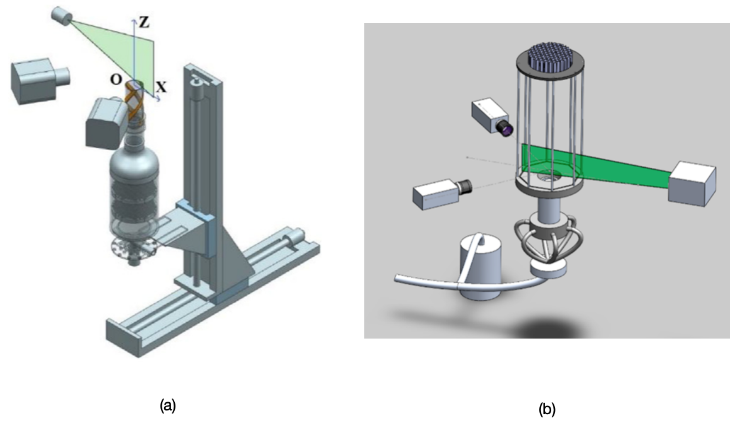

Figure 1.6: 2D3C PIV - experimental setups for: (a) plasma swirler with helical actuators (reproduced from [11]), (b) annular swirling jet (reproduced from [12]).

Nd:YAG laser and TiO_2 seeding particles were used; in [12], instead, the flow field was evaluated with a time-resolved stereoscopic PIV system consisting of two high-speed CMOS cameras, a Nd:YLF laser and DEHS (a non-resinous oil) for seeding.

Infrared Thermography

IR thermography is a non-intrusive optical tool that, as noted in [13], can be used in complex fluid flows to evaluate either wall convective heat fluxes or the behaviour of surface flow fields.
An experimental setup for the evaluation of swirling impinging jets is shown in Figure 1.7; it consists of a thin foil of constantan (a copper-nickel alloy), a swirling jet generator and an infrared camera. The constantan foil, whose temperature is measured by the IR camera, is heated by an electric current and cooled by the swirling jet impinging on its surface. For more accurate temperature measurement, the back of the impinged surface can be covered with high emissivity paint.

Data gathered by the IR camera are usually presented in a dimensionless form by using the *Nusselt number* $Nu = {}^{hD}/_{k}$ (h is the local convective heat transfer coefficient, k is the thermal conductivity of air and D is the nozzle diameter).

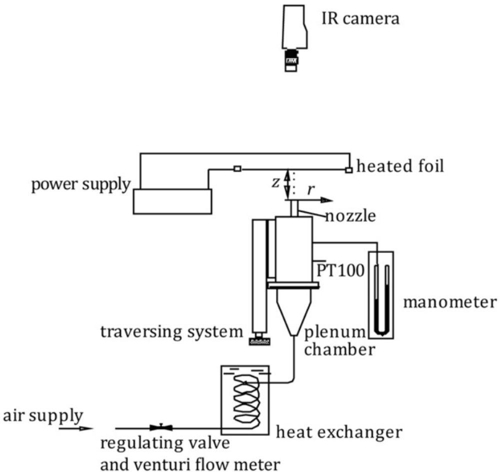

Figure 1.7: Swirling impinging jets - experimental setup (reproduced from [8]).

1.2 DBD plasma actuators

Dielectric Barrier Discharge (DBD) plasma actuators are devices that provide active flow control capability. This type of control can be distinguished from passive control by the use of an energy source to achieve and maintain the desired flow modification. In addition, they are an optimal solution for achieving fast time response and avoiding the use of moving components. As stated in [14], "the key feature of DBDs for aerodynamic purposes is the momentum transfer from accelerated ions to the surrounding neutral gas by particle-particle collisions in the underlying electric field".

1.2.1 Configuration

The basic schematic of these actuators is shown in Figure 1.8; they consist of two thin and long electrodes separated by an insulating dielectric layer; one electrode is exposed to the flow and the other is grounded and embedded in the dielectric layer. The voltages used to operate DBDs are in the range of 1 kV to 50 kV and the frequencies vary from 0.5 kHz to 25 kHz. Since the dielectric barrier can not be crossed by a DC current, it is necessary to use an AC signal, usually in the form of a sinusoidal, square or triangular wave. The application of high voltage leads to the ionization of the air above the encapsulated electrode and an ionic wind is formed as a result of the movement of electrons due to the electric field.

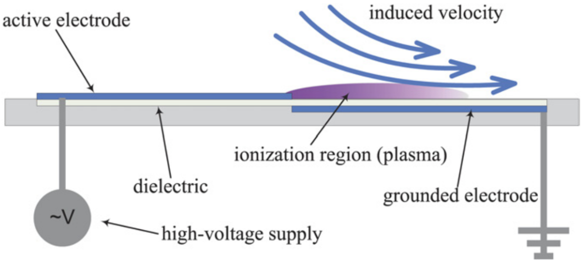

Figure 1.8: Geometrical configuration and operation of the plasma actuator (reproduced from [15]).

1.2.2 Body force characterization

The transfer of momentum from the accelerated ions to the airflow is referred as *body force field*. An experimental technique for determining the amplitude and spatial distribution of the body force exerted on the flow by a plasma actuator is described in [15] where, through the use of PIV, the evolution of the induced velocity field is measured. This technique is capable of providing the spatial and temporal resolution required to characterize the transient behaviour of the thin wall jet induced by the actuator.
This method is not always applicable, in fact as described in [10], in the case of the quartz injector, the flow field inside the plasma swirler was difficult to accurately measure due to laser reflections. In order to overcome this problem, a numerical simulation was carried out to evaluate the body force exerted by the actuation of the plasma swirler.

In [16] is reported that it is possible to express the body force per unit volume $\vec{f_B}$ in terms of the applied voltage:

$$\vec{f_B} = \rho_c \vec{E} \tag{1.9}$$

where ρ_c is net the charge density and $\vec{E}$ is the electric field. This expression can be incorporated into the Navier-Stokes equations.

1.3 Review of literature findings

This chapter presents a brief review of the results obtained in various studies regarding the active control of swirling jets by means of plasma actuators.

1.3.1 Plasma swirler with straight electrodes

It has already been pointed out that for plasma swirlers with straight electrodes, the swirl number increases linearly along the electrodes and reaches its peak at the end of the electrodes.

Effects of the applied voltage

Regarding the effects of the applied voltage, it has been observed in [10] that the increase of the applied voltage corresponds to a larger flow divergence. Furthermore, increasing the applied voltage affects the potential core region of the flow; in fact, as shown in Figure 1.9, with no voltage applied (i.e. no plasma actuation), the potential core width along the Z-axis remains almost constant. With the application of 10 kV, the potential core region begins to decrease downstream of the Z-axis, but if the applied voltage is increased high enough, the entrainment leads to the "necking" phenomenon associated with the effect of the ionic wind. This phenomenon is clearly visible in Figure 1.9(g) where the peripheral flow initially expands, then contracts and finally expands again.

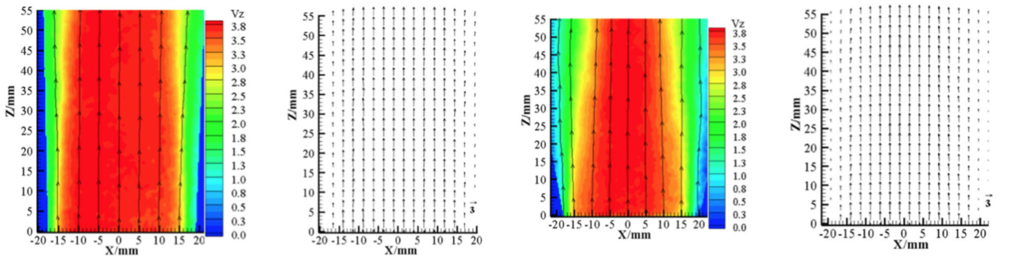

(a) Streamlines and contours of V_z (0 kV) (b) Velocity vector distribution (0 kV) (c) Streamlines and contours of V_z (10 kV) (d) Velocity vector distribution (10 kV)

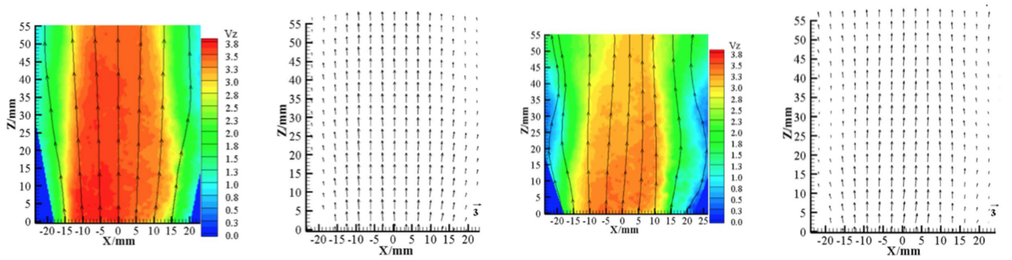

(e) Streamlines and contours of V_z (15 kV) (f) Velocity vector distribution (15 kV) (g) Streamlines and contours of V_z (20 kV) (h) Velocity vector distribution (20 kV)

Figure 1.9: Streamlines, mean axial velocity (V_z) contours and velocity vector distributions obtained through PIV measurements (reproduced from [10]).

Effects of the applied frequency

Figure 1.10 shows that the influence of the applied frequency on the mean axial velocity is weaker than the influence of the applied voltage. In fact, at $Z = 100$ mm and a constant frequency of 12 kHz, the axial velocities differ considerably for different values of the applied voltage. The measured values were: 2.51 ms^{-1} for 12 kV, 2.03 ms^{-1} for 15 kV and 1.79 ms^{-1} for 18 kV. On the other hand, when a constant voltage is applied and the frequency is varied, the difference between the values of the axial velocity is smaller; in fact, at $Z = 100$ mm and with the application of 18 kV, the measurements recorded were: 2.02 ms^{-1} for 6 kHz, 1.88 ms^{-1} for 9 kHz and 1.79 ms^{-1} for 12 kHz.

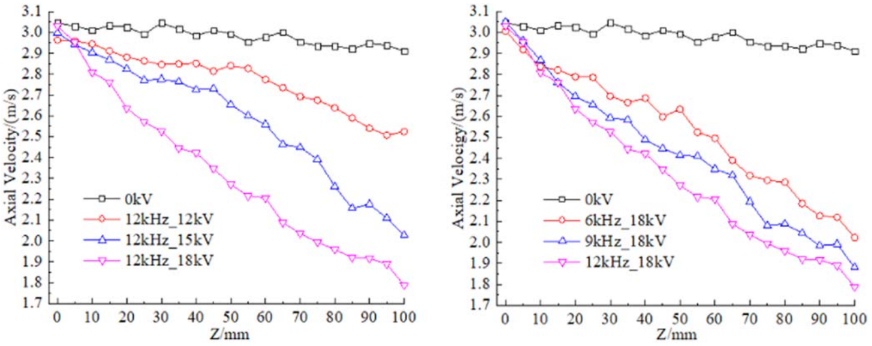

(a) Effect of applied voltage (b) Effect of applied frequency

Figure 1.10: Effect of applied voltage and frequency on the mean axial velocity (reproduced from [10]).

1.3.2 Plasma swirler with helical electrodes

The performance differences between plasma swirlers with straight electrodes and plasma swirlers with helical electrodes have been investigated in [11]. Figure 1.11 shows that without DBD actuation the flow expands slightly along the Z-axis. On the other hand, with plasma actuation, the flow expands more and a central recirculation zone (CRZ) appears at the nozzle exit. If straight electrodes are used (see Figure 1.11(b)), the CRZ has an asymmetric structure and only one vortex core can be observed. When helical electrodes were employed (see Figure 1.11(c)), it was observed in [11] that the vortex core was stronger and bigger compared to the one present in the case of straight electrodes. In addition, there was another small vortex core, indicating that the CRZ was more developed.

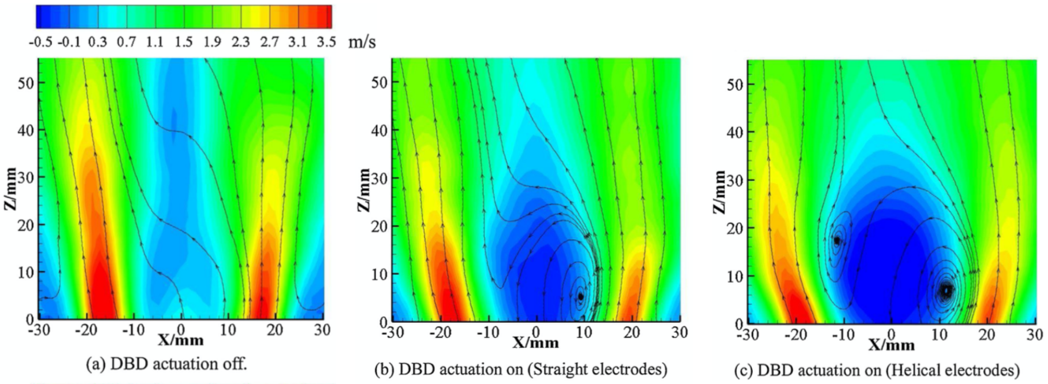

(a) DBD actuation off.
(b) DBD actuation on (Straight electrodes)
(c) DBD actuation on (Helical electrodes)

Figure 1.11: Streamlines and contours of the mean axial velocity magnitude in the XZ plane (reproduced from [11]).

In Figure 1.12 are plotted the profiles of the mean axial velocity along the centerline measured at 0 kV and at 20 kV for both straight and helical electrodes. With no voltage applied the axial velocity at the nozzle exit is 0.6 ms^{-1} and it decreases moving downstream. The profile changes consistently when plasma is applied; in fact, the axial velocity at the nozzle exit has a lower (negative) value, but as it moves downstream, its values start to increase, passing through a backward stagnation point. For plasma actuators with straight electrodes, the mean axial velocity has a minimum value of -0.45 ms^{-1} at $Z = 5$ mm and the backward stagnation point is located at $Z = 27$ mm. If, instead, helical electrodes are used, the backward stagnation point moves further downstream to $Z = 30$ mm and the minimum axial velocity is located in the CRZ at $Z = 12$ mm and decreases to -0.83 ms^{-1}.

1.3.3 Jet flow and premixed jet flame control by plasma swirler

In [9], a DBD plasma swirl injector with straight electrodes was used to investigate the feasibility of controlling and stabilizing the jet flame through this technology. Photographs of the flame with and without plasma actuation are shown in Figure 1.13. The authors observed that when the plasma swirler was activated, the flame decreased in length, changed shape from a cone to a "half ball" and became brighter.

The overall influence of swirl on the flow field can be seen in Figure 1.14. It's noticeable that the swirling motion is mainly concentrated near the wall region where the plasma actuators are placed and is very weak in the center. When the

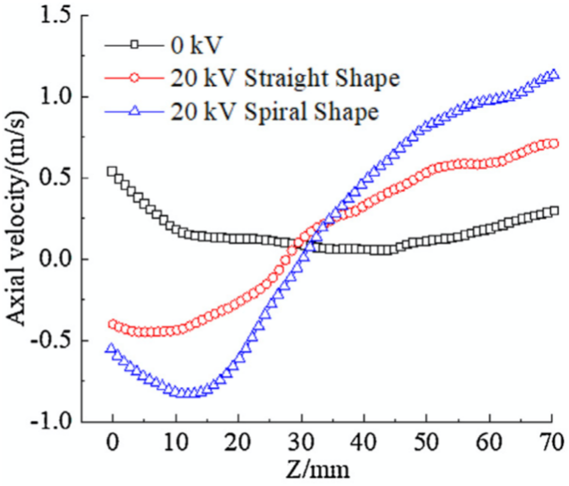

Figure 1.12: Profiles of mean axial velocity along the centerline (reproduced from [11]).

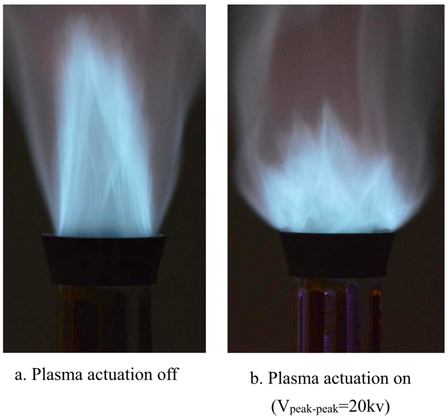
a. Plasma actuation off

b. Plasma actuation on ($V_{peak\text{-}peak}$=20kv)

Figure 1.13: Effect of DBD plasma swirl injector on jet flame (reproduced from [9]).

flow emerges from the injector, the central non-swirling flow expands due to the centrifugal force generated by the swirling motion.

1.3.4 Heat transfer in multichannel swirling impinging jets

In [8] the influence of the swirl number on the wall heat transfer distribution on a flat plate with a swirling air jet impinging was analyzed. Heat transfer maps in terms of Nusselt number were obtained by IR thermography measurement; these

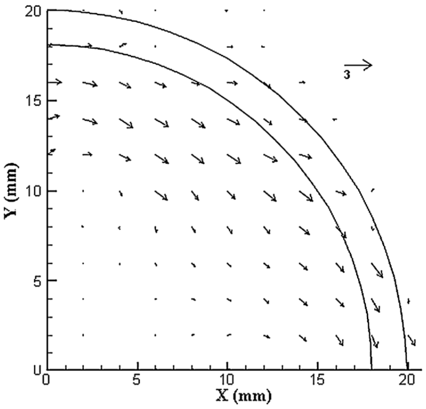

Figure 1.14: Velocity vector distributions at xy plane for a swirl number $S \approx 0.3$ (reproduced from [9]).

maps are shown in Figure 1.15. For a circular impinging jet it was observed that in region where $r/D > 3$, Nu has little dependence on the nozzle-to-plate distance as it decreases due to the increase in the boundary layer thickness in the wall jet region. In the case of the multichannel jet ($S = 0$), there is a monotonic decrease of Nu values as the nozzle-to-plate distance increases but, at short distances, this configuration provides higher heat transfer values compared to the circular impinging jet due to the creation of a central recirculation zone. Swirl number values between 0.2 and 0.4 lead to lower heat transfer values, a widening of the impinged area, but still a non-uniform Nu distribution. At $S = 0.6$ there is a region of low Nu values in the centre of the impinged plate, which may be related to a recirculation region. In the case of $S = 0.8$, the formation of four highly decentralised stagnation zones due to the vortex breakdown phenomenon is noticeable.

Thus, for a given nozzle-to-plate distance, as the swirl number increases, there is a widening of the impinged area and a reduction in the global heat transfer; at the same time, as the nozzle-to-plate distance increases, the mean heat transfer decreases independently of the swirl number.

1.4 Motivation for this work

With no moving parts, low weight, minimal power consumption and tunable control characteristics, Dielectric Barrier Discharge Plasma Actuators (DBD-PAs) are increasingly being used for active flow control in applications such as boundary layer separation, skin friction drag reduction, aerodynamic noise reduction and mixing and cooling enhancement [10]. Despite this, literature on the superposition

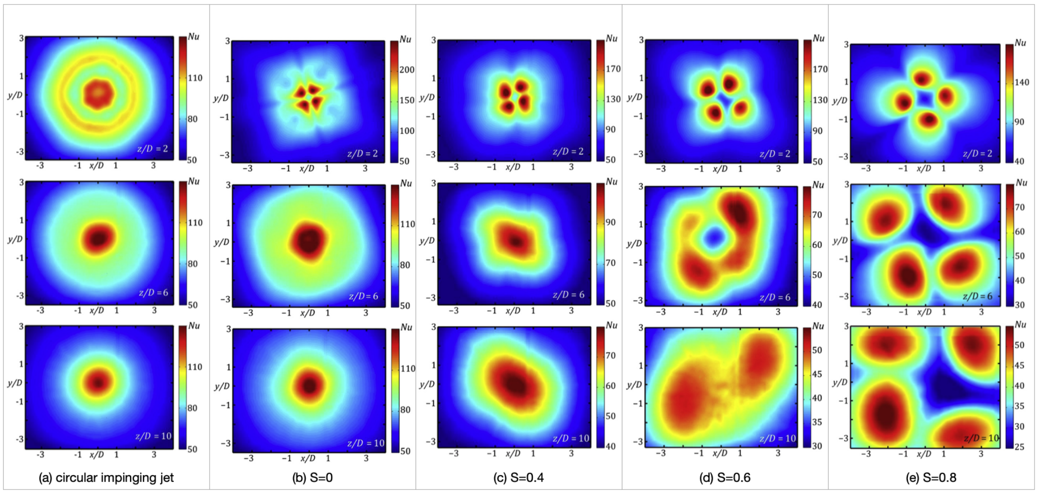

(a) circular impinging jet (b) S=0 (c) S=0.4 (d) S=0.6 (e) S=0.8

Figure 1.15: Nusselt number maps at $Re = 28000$ (reproduced from [8]).

of an azimuthal velocity component on a conventional round jet using DBD-PAs is still relatively limited.

Building upon the work of a previous Master's thesis [17], the aim of this study is to deepen the understanding and improve the control of swirling jets generated by DBD plasma actuators. To achieve this, the following goals have been identified:

- reconfiguration of the jet facility to allow Stereoscopic Particle Image Velocimetry (S-PIV) measurements;
- design of an active swirl generator with electrodes that can be triggered both simultaneously and sequentially;
- evaluation of the swirl number for each configuration;
- comparison between the jets generated by both active and passive swirl generators;
- reconstruction of three-dimensional time-averaged flow fields.

The reconfigured jet facility, which includes a newly designed nozzle and seeding system, and a detailed description of the design of the active and passive swirl generators are presented in Chapter 2. Additionally, the working principles and key features of the S-PIV technique are discussed.

In Chapter 3, for each configuration, the flow field at a distance of $z/D = 0.5$ from the exit section is analyzed to estimate the swirl number. A comparison between jets generated by different methods is then made by analysing the vorticity, the radial distribution of the velocity components and the circulation. Subsequently, velocity fields measured at different distances from the exit section are interpolated to reconstruct the three-dimensional time-averaged flow field, providing a detailed description of the evolution of the jets along their axis. Lastly, with regard to the sequential triggering of the DBD-PAs, the preliminary results of this novel approach to induce the swirling motion are briefly presented in Chapter 4.

Chapter 2

Experimental setup

The experiments were carried out at the Modesto Panetti Laboratory, within the Aerospace Department of Politecnico di Torino.
In this work, the three-dimensional flow field of the swirling jet is measured using Stereoscopic Particle Image Velocimetry (PIV). This chapter details the experimental setup used to conduct these measurements and outlines the working conditions, as well as the preliminary steps required to calibrate the system.

2.1 Jet Facility

Given the need to evaluate various cases in this work, many of which required changes to the setup configuration, a new nozzle was specifically designed and 3D printed for the jet facility. The convergent profile of the nozzle was determined based on Vitoshinski's equation (2.1), which provides the radius distribution ($r(x)$) along the axial position (x), given specified initial and exit radii (R_i and R_e) as well as the total length (L) of the nozzle [18].

$$r(x) = \frac{R_e}{\sqrt{1 - \left[1 - \left(\frac{R_e}{R_i}\right)^2\right] \frac{\left(1 - \frac{x^2}{L^2}\right)^2}{\left(1 + \frac{x^2}{3L^2}\right)^3}}} \tag{2.1}$$

A flange at the nozzle's exit section, along with a 3D-printed support, allowed for the easy installation of various inserts, such as the short pipe and the passive and active swirl generators, downstream of the nozzle. In Figure 2.1 is shown a 3D CAD model of this setup.
A key feature of this new setup is the inclusion of static pressure probes positioned at the inlet and exit sections of the nozzle, as well as at the exit section of the inserts. This configuration allowed the measurements to be carried out at a fixed pressure

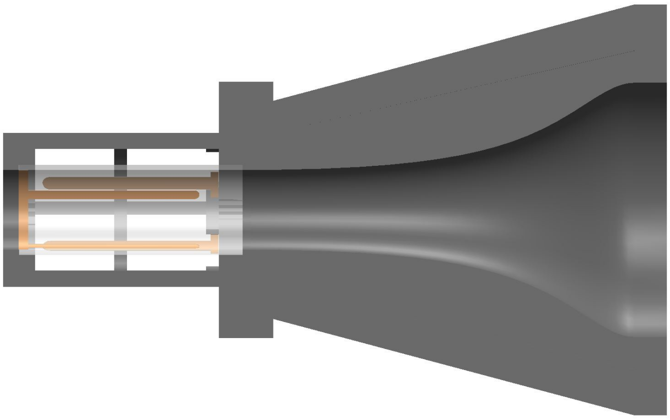

(a)

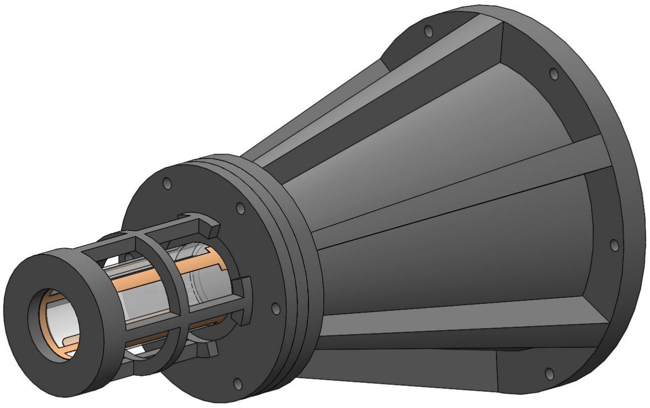

(b)

Figure 2.1: 3D CAD model: (a) Section (detail of the Vitoshinski nozzle) and (b) Complete setup.

drop. Compressed and filtered air is supplied by a pneumatic line, regulated by a system of two valves: one for coarse control and the other for fine pressure control. For the Stereo-PIV measurements, a Laskin nozzle is placed between the pneumatic line and the jet facility to ensure that all the air from the nozzle is filled with nebulised seeding particles. For this work, the Laskin nozzle used is the PIVlight30 model and the seeding particles are PIVLIGHT, both supplied by PIVTEC GmbH.

Given that the surface finish of the nozzle exhibited some roughness due to the nature of 3D printing, a hot-wire measurement campaign was conducted to assess the symmetry of the jet. As shown in Appendix A, the jet was found to be axisymmetric.

2.2 Stereoscopic Particle Image Velocimetry

2.2.1 Overview

In the Stereoscopic PIV two cameras are employed to record simultaneous off-axis views of the region of interest allowing to evaluate the out-of-plane component. As explained in [19], measuring three-dimensional particle displacements with a single camera is not feasible because there are three unknowns $(\Delta x, \Delta y, \Delta z)$, while a single view provides only two equations. By introducing a second camera, a third equation can be obtained which allows the three unknown displacements to be determined.

Following the classification proposed in [20], where a flow velocimetry technique is labeled as (k, l, m), with $k = 1, 2, 3$ indicating the number of velocity components measured, $l = 0, 1, 2, 3$ representing the number of spatial dimensions in the measurement domain, and $m = 0, 1$ signifying either instantaneous or continuous time recording, Stereoscopic PIV can be classified as a $(3, 2, 0)$ method.

Two main classes of stereoscopic systems can be identified: translational (lateral displacement) and rotational (angular displacement). In the former, the cameras' axes are parallel to each other and orthogonal to the light sheet. Its simple configuration, with the lenses and measurement plane parallel to each other, offers several advantages, such as a uniform magnification factor, good image focus without the need to excessively reduce the lens aperture, and easy alignment of the two camera views. However, this setup comes at the cost of a limited common area viewed by both cameras and a maximum off-axis angle θ between the center of the measurement plane and the center of each lens. This limitation is not present in rotational systems, in fact, as shown in Figure 2.2, the two cameras are rotated so that their axes intersect in the proximity of the measurement plane. Increasing the off-axis angle θ improves the accuracy of out-of-plane component evaluation, but results in non-uniform magnification across the field of view. Moreover, to satisfy the Scheimpflug condition - which requires the object, lens, and image planes to be collinear in order to keep the entire measurement plane in focus - it is necessary to rotate the image plane by an angle α relative to the lens plane.

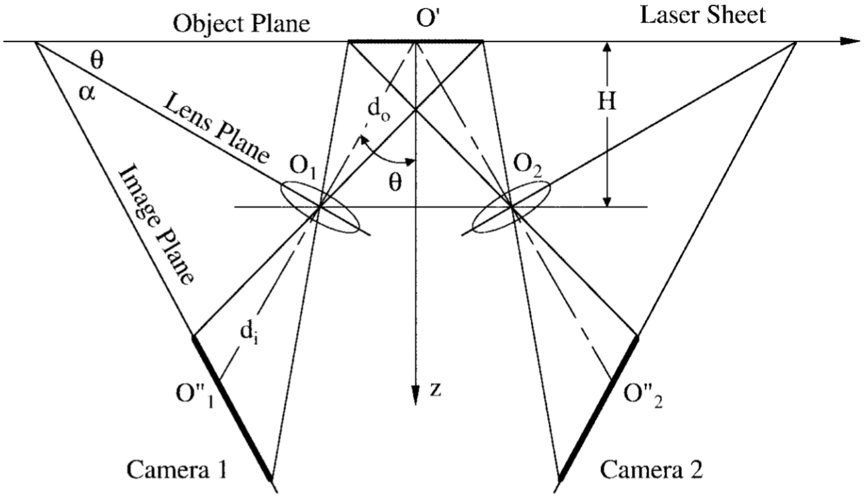

Figure 2.2: Stereoscopic PIV: rotational system - angular displacement method (reproduced from [19]).

Calibration

Once the system is configured, a process called reconstruction is used to evaluate the displacement between each image plane and the measurement plane, enabling the acquisition of three-dimensional data. One possible reconstruction method is the 2D calibration method, which requires positioning a calibration target (typically a plate with dots arranged in a Cartesian grid) in the object plane, ensuring that the target's face coincides with the laser sheet. This calibration allows any point in the image plane to be uniquely mapped to its corresponding point in the object plane. After removing the calibration plate, stereo images of the flow can be acquired and the data interpolated to obtain $\Delta x, \Delta y$ and Δz.

The reconstruction method requires the calibration target to be perfectly aligned with the centre of the measurement plane, but as explained in [21], this is a difficult task to achieve in practice. Therefore, even a slight misalignment between the calibration target and the laser sheet leads to a mismatch between the areas actually captured. The process of correcting this misalignment is known as *disparity correction*, which relies on PIV recordings from both cameras. The images are "dewarped" based on their projection coefficients, and a cross-correlation is performed between the two views. The resulting displacement field represents the disparity between the views and is used to adjust the mapping coefficients, thereby correcting the misalignment. The accuracy of the disparity map can be further improved by incorporating an entire sequence of images.

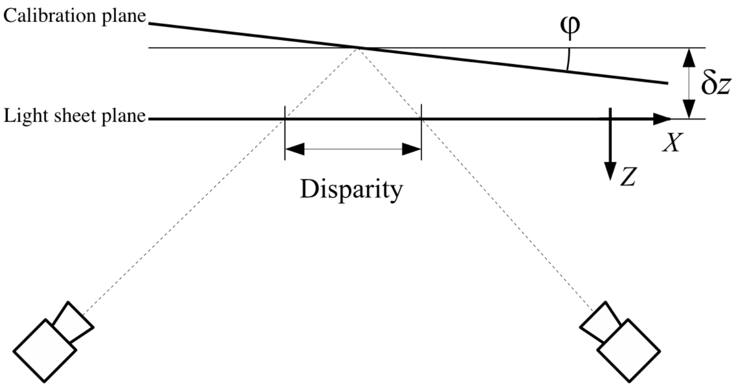

Figure 2.3: Example of misalignment between the calibration target and the laser sheet (reproduced from [21]).

Figure 2.5 shows an example of cross-correlation planes obtained during the disparity correction process. The peaks exhibit an elliptical shape, with the major axis aligned along the plane spanned by the camera axes. This occurs because the laser sheet has a finite thickness, making it impossible - even in the case of perfect alignment - for the particle images to perfectly coincide between the two views. The thickens of the laser sheet directly influences the width of the peaks.

Tracer particles

Unlike other techniques such as hot-wire anemometry or pressure probes, PIV provides a direct measure of velocity. However, the velocity measured is the velocity of the particles within the flow, not the velocity of the fluid itself. Hence, it is important to select particles with fluid-mechanical properties that do not lead to a significant discrepancy between fluid and particle motion.
The motion of a particle is governed by the Basset equation:

$$\left(\frac{\pi D_p^3}{6}\rho_p\right)\frac{du_p}{dt} = 3\pi\mu_f D_p(u - u_p) \tag{2.2}$$

where D_p, ρ_p, u_p are the diameter, density and velocity of the particle respectively, while μ_f is the dynamic viscosity of the fluid and u is its velocity. From equation

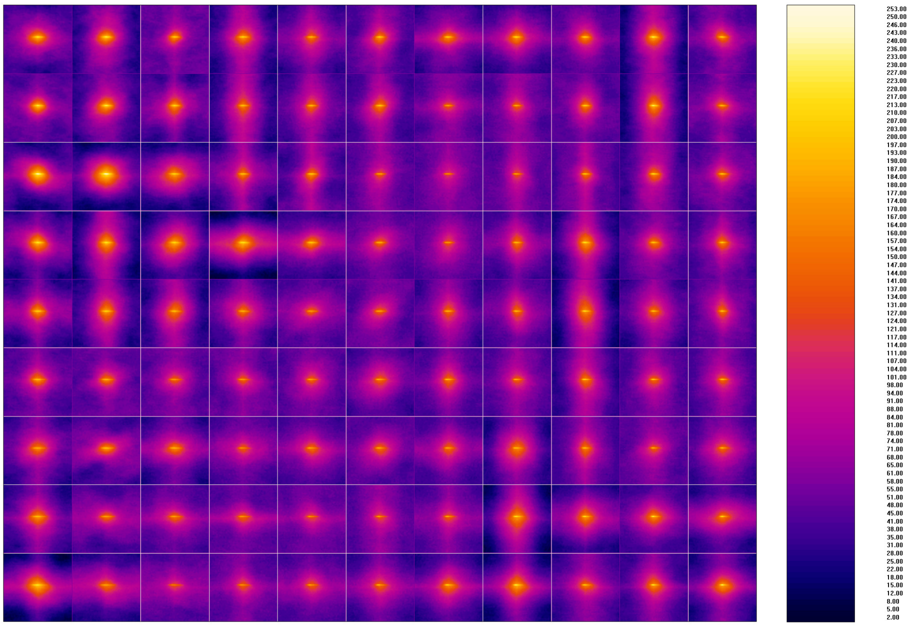

Figure 2.4: Example of cross-correlation planes obtained during disparity correction.

(2.2), it is possible to derive the acceleration of the particle:

$$\frac{du_p}{dt} = \frac{18\nu_f(u - u_p)}{D_p^2(\frac{\rho_p}{\rho_f})} \tag{2.3}$$

In order to make the particle motion follow the flow field, the following parameters must be respected:

- The density of the particles (ρ_p) has to be similar to the density of the fluid (ρ_f), ensuring that $\frac{\rho_p}{\rho_f} \approx 1$
- The diameter of the particles D_p has to be on the order of a few microns.

Following the Basset equation, it is possible to derive a dimensionless parameter called the *Stokes number*, which is defined by the ratio between two characteristic times:

$$St = \frac{t_p}{t_0} \tag{2.4}$$

where t_0 is a characteristic time of the flow field (such as the ratio between a characteristic velocity and a reference length) and t_p is defined as *relaxation time* and indicates the particle's tendency to reach velocity equilibrium within the fluid. The relaxation time can be expressed as:

$$t_p = \frac{D_p^2 \rho_p}{\mu_f} \tag{2.5}$$

The particle follows the flow field only if the following condition is satisfied:

$$St \ll 1 \tag{2.6}$$

Post-processing

Once the flow field is seeded with particles, image acquisition can begin. The seeding particles reflect the laser light, making them visible in the captured images. In fact, each PIV snapshot is a dark image filled with illuminated dots, representing the light reflected by particles at their positions as captured by the camera at each instant. Thus, it is possible to describe a PIV snapshot as a map of light intensity distribution. From the position of the illuminated dots in the PIV image, the displacement $\Delta\vec{s}$ of the particles is evaluated using autocorrelation and cross-correlation algorithms.
The images in a non-time-resolved PIV system can be either single-exposed or multi-exposed. A brief explanation of the working principle of the former is given in the following, as a non-time-resolved, single-exposed stereoscopic PIV was used in this study. In this system, the measurement field is illuminated by the laser sheet at an imposed Δt, which depends on the characteristic velocity of the field to be measured. A synchronizer ensures that snapshots are captured by the cameras each time the laser pulses. The displacement of particles is then calculated from a pair of snapshots (one pair per camera). In fact, by comparing the pair of images, it is possible to observe that the particles result to be displaced by a certain value $\Delta\vec{s}$.

Knowing the values of $\Delta\vec{s}$ and Δt, it is possible to evaluate the velocity vector $\vec{V} = \frac{\Delta\vec{s}}{\Delta t}$. A post-processing algorithm is used to divide the PIV image into small interrogation windows. For each pair of PIV images, the algorithm selects corresponding interrogation windows (one from each image). It then computes the cross-correlation function of the intensity levels ($f(h,k)$) within these pairs of interrogation windows. The cross-correlation function, reported below, reaches its peak at the point of maximum probability. This point is defined by the distance between the origin and the centroid of the maximum intensity peak. This distance corresponds to the previously unknown displacement $\Delta\vec{s}$.

$$R_{j,j+1}(r_1, r_2) = \sum_{h=1}^{\Delta h} \sum_{k=1}^{\Delta k} f_j(h,k) f_{j+1}(h + r_1, k + r_2) \Delta h \Delta k \tag{2.7}$$

By iterating this process through all the snapshots acquired, it is possible to evaluate the mean velocity field.

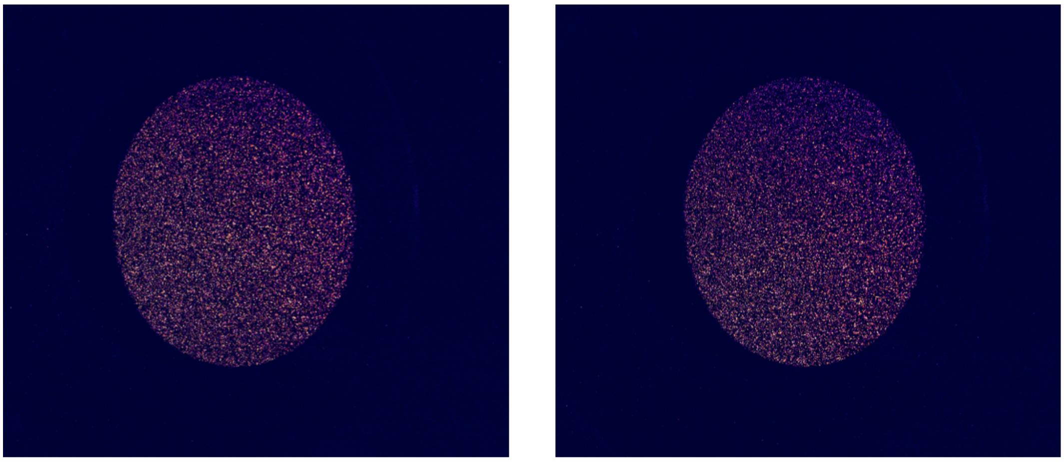

Figure 2.5: Example of a non-time-resolved, single-exposure stereoscopic PIV snapshot pair acquired from a single camera. The left image is acquired at t_0 and the right at $t_0 + \Delta t$.

2.2.2 S-PIV setup

The S-PIV setup consists of two sCMOS cameras (Andor Zyla ZL41 5.5 Mpx, with a sensor of 2560 x 2160 px), a Nd:YAG laser source (Dantec Dynamics 15 Hz, 200 mJ/pulse laser), and a series of mirrors and lenses. Each camera is equipped with a Tokina lens (macro 100 f 2.8 D), a green filter, and a LaVision Scheimpflug corrector adapter to ensure that the entire measurement plane is in focus. The laser beam is directed toward the jet facility using two mirrors, each deflecting the beam by 90°. It then passes through two spherical lenses (LD1170 $f = -75mm$ and LA1509 $f = 100mm$) and a cylindrical lens (LK1336RM-A $f = -50mm$) to generate the laser sheet. The system is synchronized using a National Instruments PCI-662 board.

Figure 2.6.a and Figure 2.6.b show the lenses setup used to generate the laser sheet and the cross-plane configuration of the cameras, respectively. The cameras are positioned at an angle of approximately 55° relative to the measurement plane.

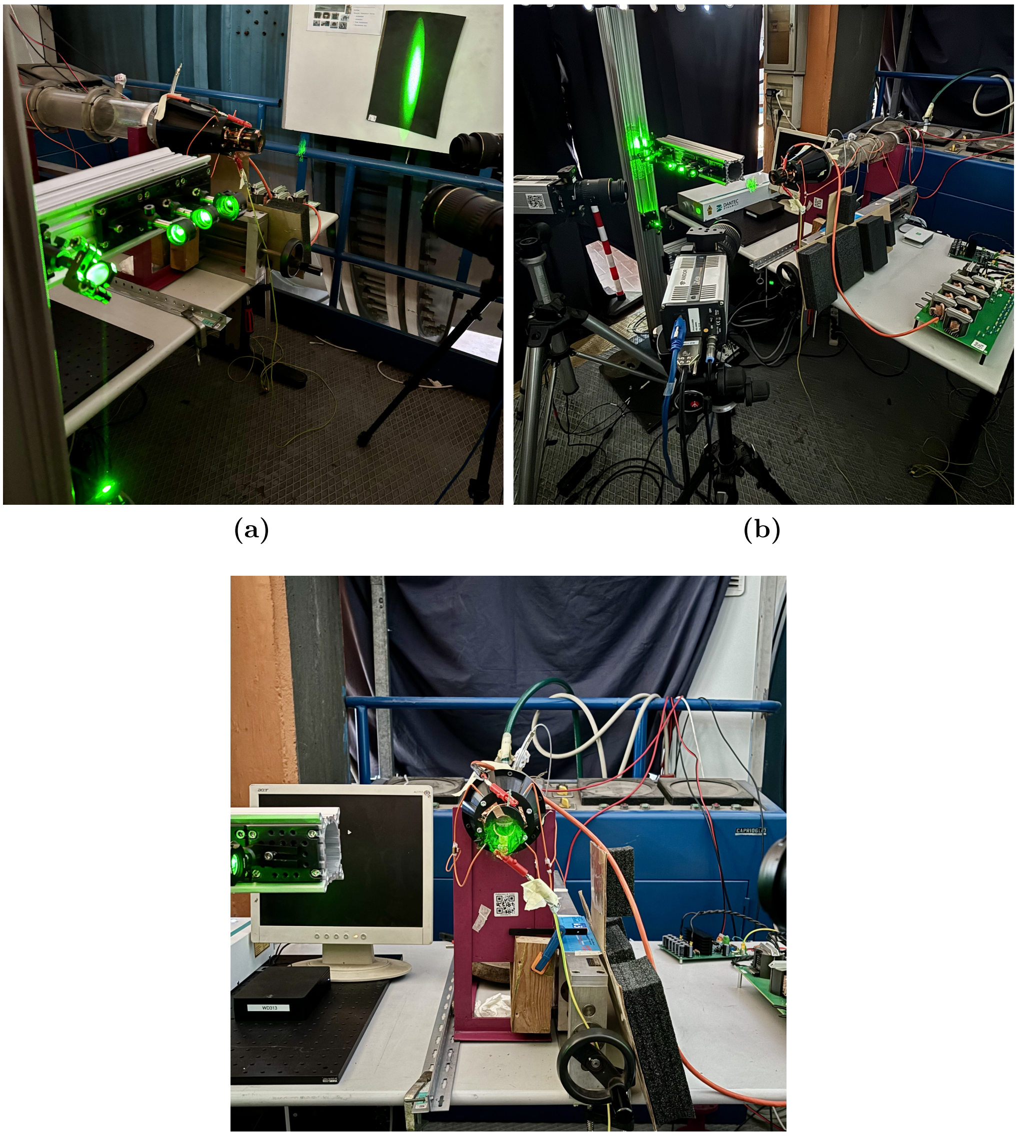

(a) **(b)**

(c)

Figure 2.6: S-PIV setup: (a) Lenses ans laser beam, (b) Cross-plane configuration of the cameras, and (c) Example of the measurement plane illuminated by the laser sheet.

The calibration was performed in the plane corresponding to an $z/D = 0$ distance from the exit section of the inserts, which corresponds to the plane of the laser sheet. By mounting the jet facility on a linear stage, all measurements were performed without moving the optical and laser apparatus, but simply by varying the z/D distance between the exit section and the laser sheet. To calibrate the stereoscopic camera system, a 3D calibration plate from LaVision was used with a defined separation of the two calibration planes ($1mm$) and dots spacing ($2.5mm$).

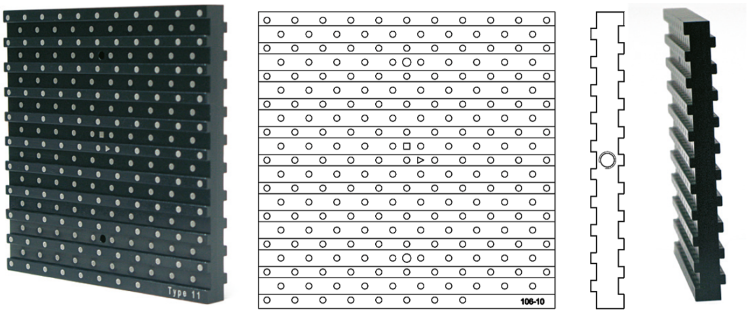

Figure 2.7: 3D calibration plate

2.3 Swirl generators

In this work, both active and passive swirl generators were utilized. This section offers a brief description of their characteristics.

2.3.1 Passive swirl generators

The passive method used to induce the swirling motion was based on guided vanes designed to force the flow to follow a helical path. Taking into account the results obtained in [17], three low Swirl numbers (0.1, 0.2 ,0.3) were selected and the geometry of the helical inserts was derived from the following empirical equation which was presented in [5].

$$S = \frac{2}{3}\frac{\left[1-\left(\frac{d}{D}\right)^3\right]}{\left[1-\left(\frac{d}{D}\right)^2\right]}\tan\theta \tag{2.8}$$

As shown in Figure 2.8, D represents the internal diameter of the injector, d is the hub diameter, and θ is the swirl angle. By fixing the values of D, d and L, it was possible to derive the remaining geometric parameters corresponding to each selected Swirl number.

$$\tan\theta = \frac{3}{2}\frac{\left[1-\left(\frac{d}{D}\right)^2\right]}{\left[1-\left(\frac{d}{D}\right)^3\right]}S \tag{2.9}$$

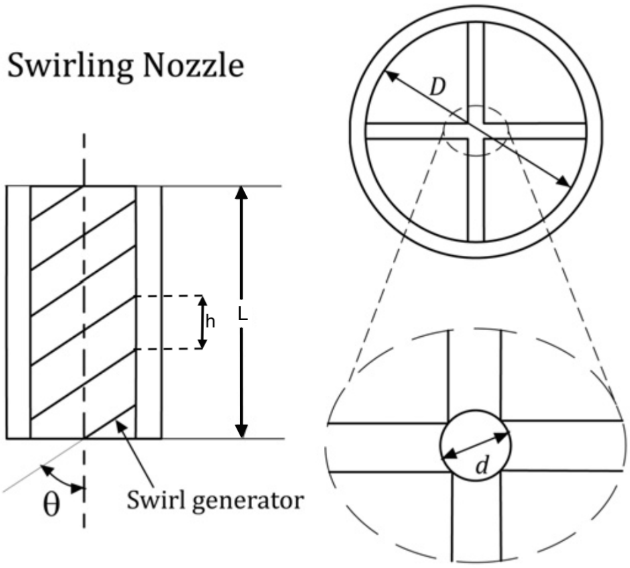

Figure 2.8: Geometry of a passive swirl generator (reproduced from [8]).

$$h = \frac{D}{\tan\theta} \tag{2.10}$$

One complete helical revolution corresponds to an axial length increase of $4h$. Given this, the number of revolutions, R, for a fixed length L is:

$$R = \frac{L}{4h} \tag{2.11}$$

S	L $[mm]$	D $[mm]$	d $[mm]$	$\tan\theta$	R
0.1	70	25	2.83	0.1483	0.10381
0.2	70	25	2.83	0.2966	0.20761
0.3	70	25	2.83	0.4449	0.31142

Table 2.1: Geometric parameters of passive swirl generators

With all the geometric parameters defined for each passive swirl generator, the designs were modeled in a CAD software (specifically SolidWorks) and subsequently 3D printed.

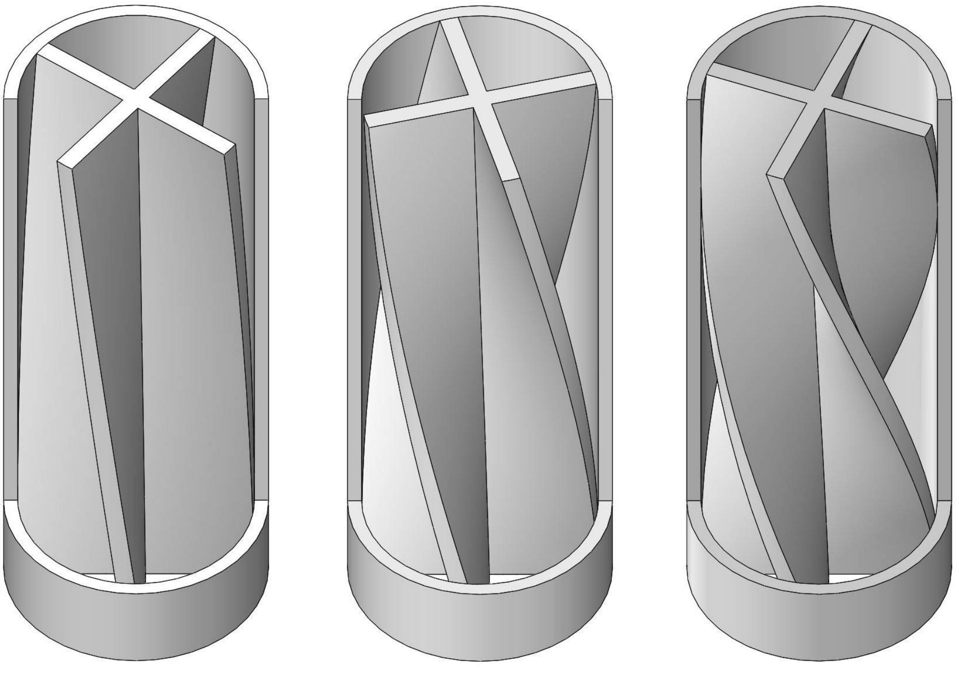

(a) **(b)** **(c)**

Figure 2.9: Passive swirl generators - detail of helical inserts: (a) $S = 0.1$, (b) $S = 0.2$, and (c) $S = 0.3$.

2.3.2 Active swirl generators

With respect to the active swirl generators, their design followed the approach presented in [9], where four pairs of DBD-PAs were installed along the axial direction of the injector (a short pipe) and evenly spaced around its circumference. Given the preliminary phase of this study, the injectors were 3D printed using a PLA filament and their walls were used as dielectric barriers for the PAs.

Each DBD-PA consisted of two copper foil tape electrodes, both 0.35 *mm* thick. The narrower electrode, measuring 3 *mm* in width and 50 *mm* in length, was placed inside the injector and exposed to the air. The wider electrode, 5 *mm* wide and 50 *mm* long, was positioned externally and insulated with three layers of Kapton tape. The injector wall had a thickness of 1.5 *mm*. Figure (2.10) shows a 3D CAD model of the active swirl generator.

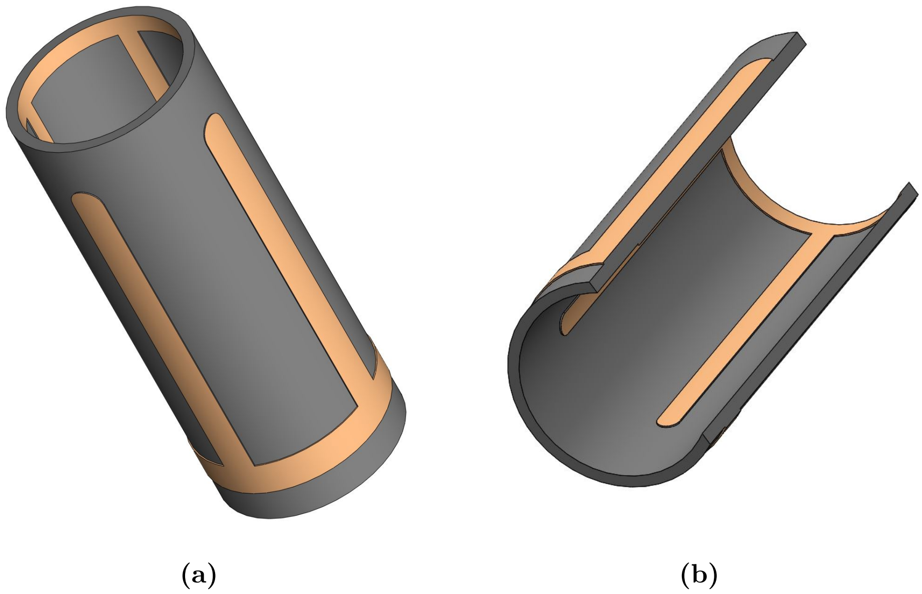
(a) (b)

Figure 2.10: Active swirl generator - 3D CAD model: (a) External view and (b) Section (detail of the configuration of the electrodes).

2.3.3 Electrical configuration

Two different electrical configurations were used: one to allow simultaneous activation of all DBD-PAs and another to test their sequential triggering. In both cases, the exposed electrodes were grounded, while the encapsulated electrodes were connected to the high voltage.

Simultaneous ignition

To ignite the four DBD-PAs simultaneously, all the encapsulated electrodes were connected to a single high-voltage generator, the GBS Elektronik GmbH Minipuls 4. This device consists of a full-bridge converter that generates a powerful low-voltage square wave, which is stepped up by a transformer cascade to a maximum of 20 kV and filtered to produce a sine-like waveform. The bridge converter was connected to both a DC power supply (Voltcraft VSP-2410) and a function generator (RS PRO AFG-21005). An oscilloscope (RS PRO RSDS1102CML+) was used to monitor the high-voltage AC signal generated by the transformer cascade.

For this configuration, three distinct sets of operating conditions, defined by peak-to-peak voltage (V_{pp}) and frequency (f), were evaluated. These conditions are presented in Table 2.2.

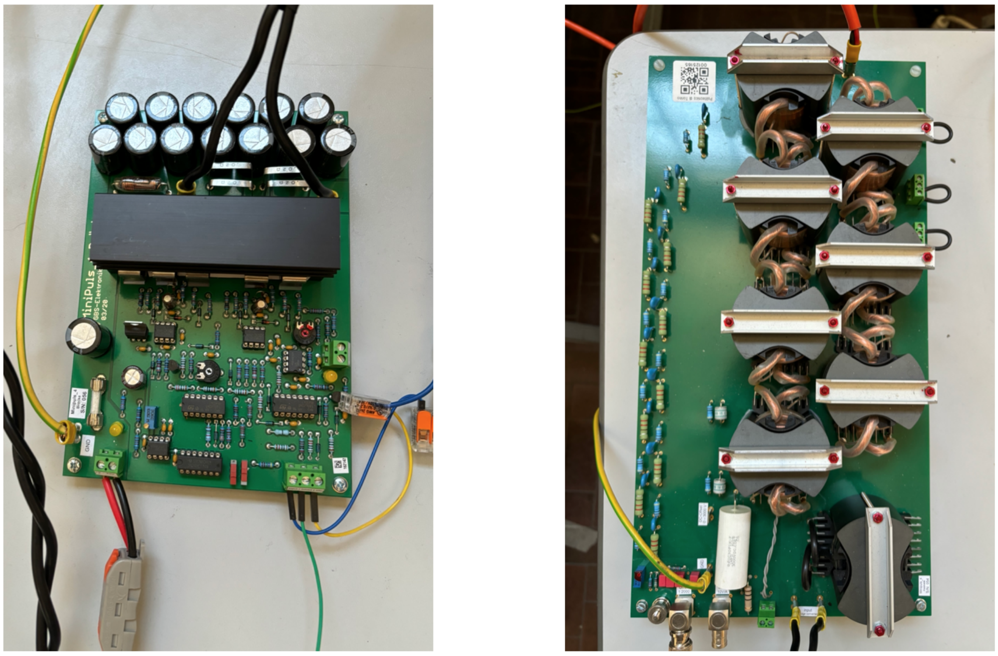

Figure 2.11: GBS Elektronik GmbH Minipuls 4 - the bridge converter on the left and the transformer cascade on the right.

Configuration	V_{pp} $[kV]$	f $[kHz]$
1	10	17
2	12	15
3	14	14

Table 2.2: Operating conditions for simultaneous ignition.

Sequential triggering

To achieve sequential triggering, the system was reconfigured by dividing it into four independently controlled DBD-PAs. Each encapsulated electrode was connected to its own dedicated GBS Elektronik GmbH Minipuls 4 generator to ensure isolation between the actuators, with each unit powered by a separate power supply. Additionally, each bridge converter was connected to a dedicated voltage output channel of a National Instruments module, allowing individual control of the DBD-PAs. By generating an output voltage signal greater than 1.5 V on a specific channel, it was possible to inhibit the activation of the corresponding DBD-PA.
The peak-to-peak voltage ($V_{pp} = 10$ kV) and frequency ($f = 15$ kHz) were held

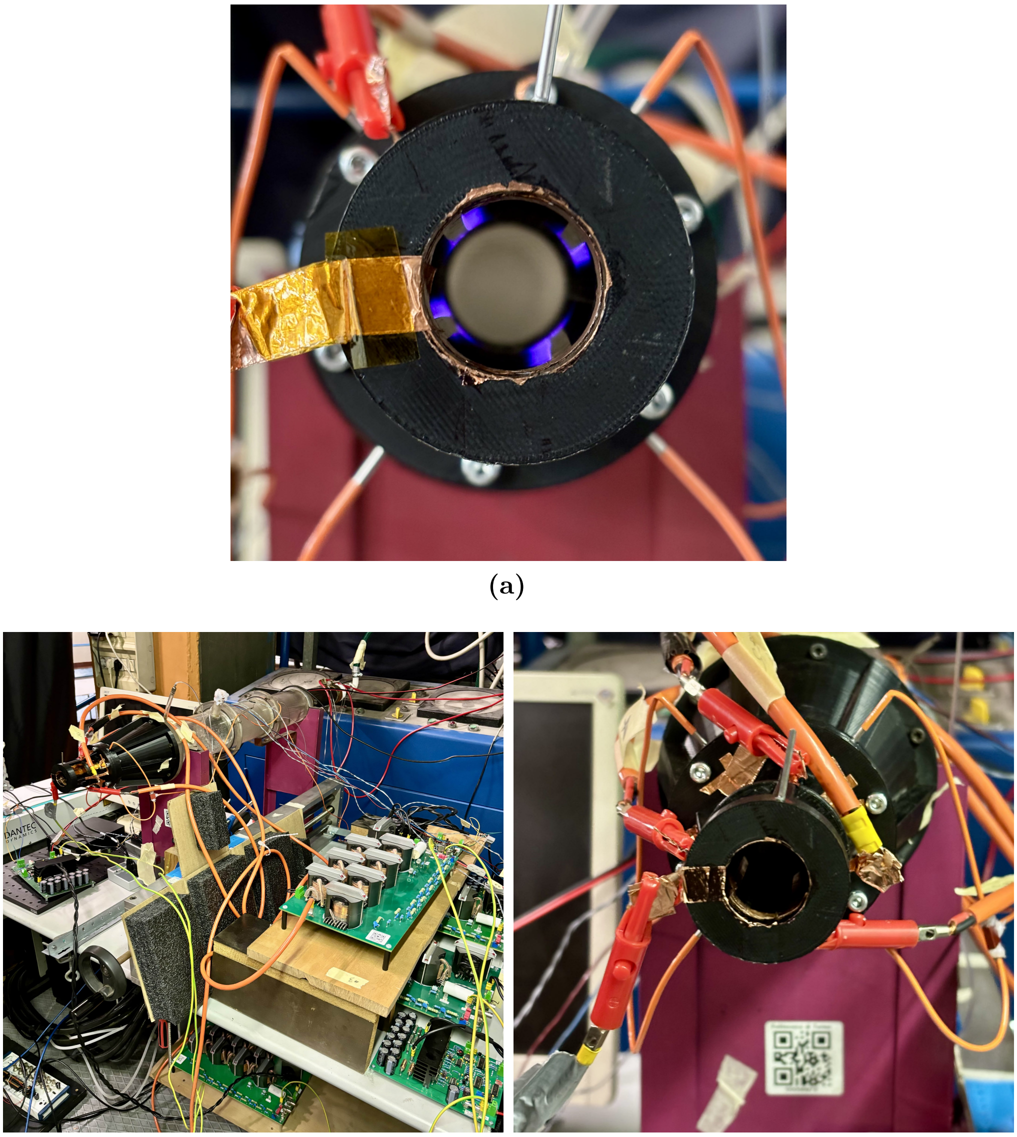

(a)

(b) **(c)**

Figure 2.12: Active swirl generators: (a) Plasma generated by the four DBD-PAs simultaneously ignited, (b) and (c) Setup for the sequential triggering.

constant for this configuration, while two different cases were tested, each characterized by a different triggering frequency $f_{DBD-PAs}$. Following the methodology outlined in [22], the S-PIV system was synchronized with the DBD-PAs in order to perform phase-averaged measurements. The S-PIV images were acquired at a frequency f_{S-PIV}, which is determined by the following equation:

$$f_{S-PIV} \quad = \quad \frac{f_{DBD-PAs}}{\frac{1}{N_{div}} + n} \tag{2.12}$$

where N_{div} is the number of sampled phases and n is the sampling period of the DBD-PA ignition, with a phase shift of $360°/N_{div}$. The operating parameters are reported in Table 2.3.

Configuration	V_{pp} $[kV]$	f $[kHz]$	N_{div}	n	$f_{DBD-PAs}$	f_{S-PIV}
1	10	15	20	1	10.5525	10.05
2	10	15	20	1	7.035	6.7

Table 2.3: Operating parameters for sequential triggering.

Chapter 3

Results

In this chapter, the main results concerning the simultaneous ignition of the four DBD-PAs are presented. Unless otherwise specified, a cylindrical polar coordinate system is employed, where the velocity components in the axial (z), radial (r), and tangential (θ) directions are denoted as w, V_r, and V_θ, respectively. The axial direction is parallel to the jet axis. All measurements were conducted under a constant pressure drop of $\Delta P = 25.8\ Pa$ between the inlet and exit sections of the Vitoshinski nozzle.

3.1 Swirl number evaluation

To evaluate the Swirl number (S), experimental measurements were conducted near the nozzle, specifically at a distance of $z/D = 0.5$ from the exit section. The expression used for its calculation follows the formulation presented in [9]:

$$S = \frac{\displaystyle\int_0^R V_\theta w 2\pi\rho R r^2\, dr}{R \cdot \displaystyle\int_0^R w^2 2\pi\rho r\, dr} \tag{3.1}$$

Given the different velocity fields produced by the different swirl generation methods, two separate approaches were adopted to automatically determine the jet center. For the passive swirl generators, a series of search windows were defined, and within each, the vector sum of the x and y velocity components was computed. The jet center was then assigned to the window with the smallest calculated value. In contrast, for the active swirl generators, the center was located at the centroid of the central region, characterized by a uniform axial velocity. Figures 3.1 and 3.2 show the mean field for each velocity components across the different cases, including the perimeter and center of the jet.

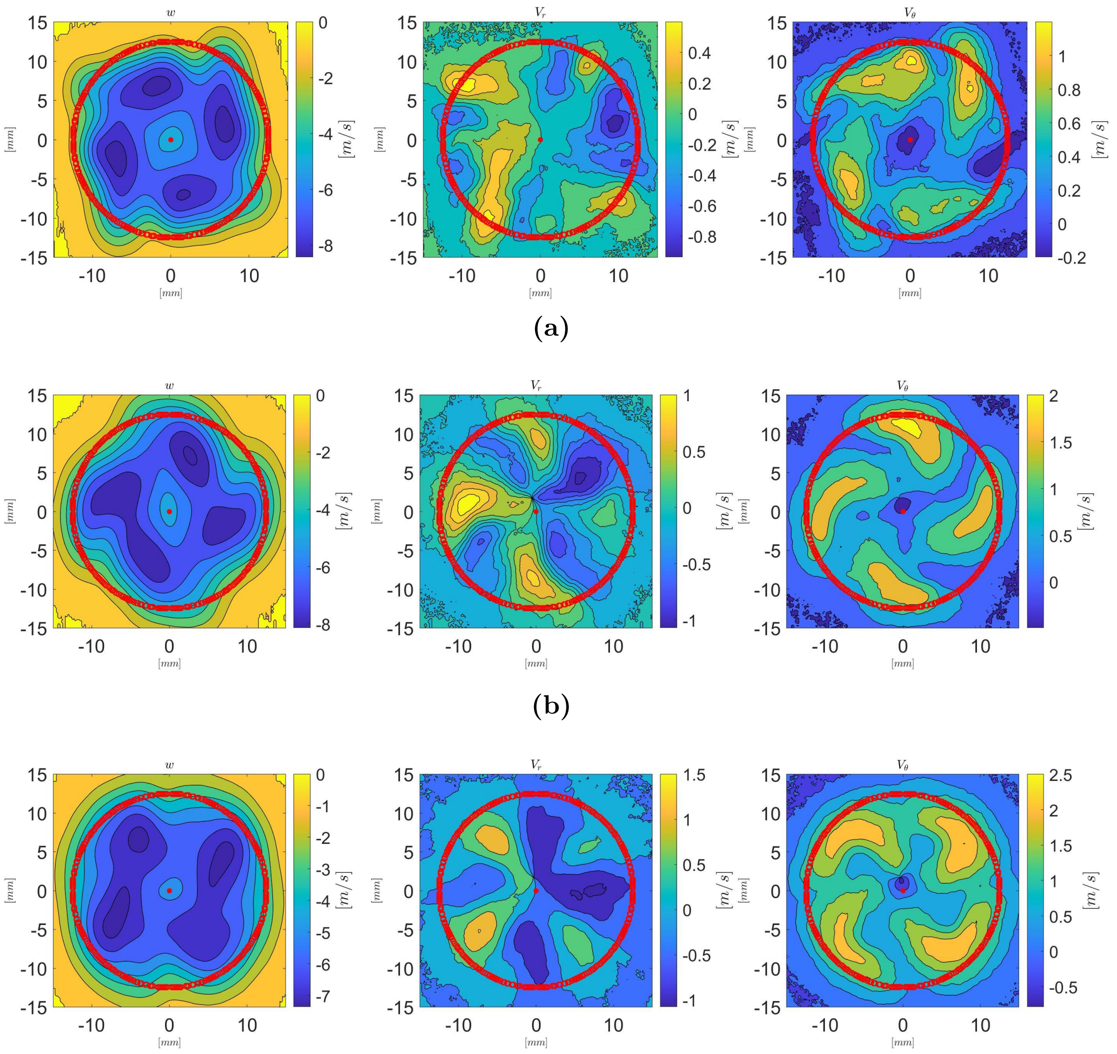

(a)

(b)

(c)

Figure 3.1: Mean axial, radial, and tangential velocity fields at $z/D = 0.5$ - Passive swirl generators: (a) $S_{\text{design}} = 0.1$, (b) $S_{\text{design}} = 0.2$, and (c) $S_{\text{design}} = 0.3$.

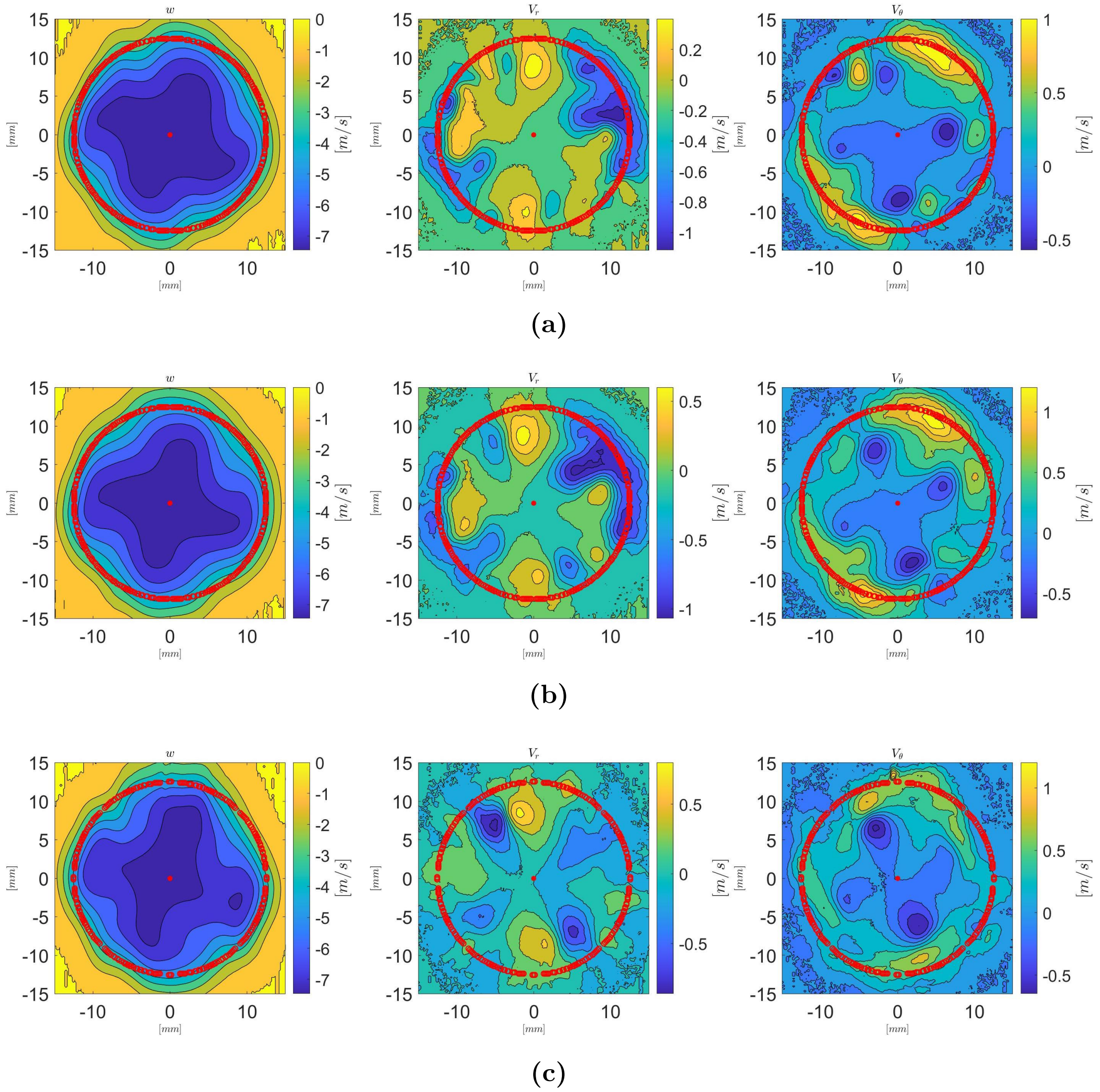

(a)

(b)

(c)

Figure 3.2: Mean axial, radial, and tangential velocity fields at $z/D = 0.5$ - Active swirl generators: (a) $V_{\text{pp}} = 10\ kV$, (b) $V_{\text{pp}} = 12\ kV$, and (c) $V_{\text{pp}} = 14\ kV$.

The calculated swirl numbers are reported in Table 3.1. Two significant observations can be made from the data. First, the methodology used to evaluate the swirl number proves to be effective; in fact, in the cases involving passive swirl generators, there is a strong correlation between the designed swirl number S_{design} and the calculated swirl number S. Second, it is noteworthy that the values obtained with the active swirl generators are consistently lower than those achieved with the guided vanes.

Swirl Generation Method	**Case**	**Swirl Number (S)**
Guided Vanes	$S_{\text{design}} = 0.1$	0.1107
	$S_{\text{design}} = 0.2$	0.2059
	$S_{\text{design}} = 0.3$	0.2858
DBD-PAs	$V_{\text{pp}} = 10$ kV	0.0665
	$V_{\text{pp}} = 12$ kV	0.0821
	$V_{\text{pp}} = 14$ kV	0.0685

Table 3.1: Calculated Swirl Numbers.

To gain a deeper insight into the reasons for this difference, it is useful to compare the vorticity and the radial distribution of both the velocity components and the circulation (Γ) across all cases.

3.1.1 Radial distributions

Given the non-homogeneity of the velocity field - particularly in cases where DBD-PAs were used, which can be attributed to the handmade nature of these swirl generators - it was considered more appropriate to analyze the radial distributions of the mean quadrant. This mean quadrant is derived by partitioning the velocity fields into four sections, each spanning 90 degrees, and averaging the corresponding values across these sections. Figures 3.3 to 3.8 present the resulting normalized velocity fields and the corresponding radial distributions for each velocity component, with normalization based on the maximum axial velocity measured in each case. Additionally, the radial distributions at 22.5°, 45°, and 67.5° are highlighted in blue, green, and red, respectively, to emphasize the variation of velocity across these angular positions.

A close examination of the fields corresponding to the radial and tangential velocity components reveals the presence of larger, more developed regions with higher velocity magnitudes in the cases corresponding to the passive swirl generators (see Figures 3.5 and 3.7). Hence, the induction of a higher tangential velocity, as seen in equation 3.1, results in a higher swirl number due to the direct relationship between the tangential velocity and the numerator in the equation.

By averaging the radial distributions across the mean quadrant, a representative radial profile can be derived for each case, thus providing a more comprehensive understanding of the flow characteristics and allowing a direct comparison between the different cases. As will be shown in the following sections, key differences emerge over the radial length when comparing the radial profiles of the swirling jets generated by both passive and active methods with those of the axisymmetric jet. These differences highlight the influence of the swirl generation mechanism on the overall jet behaviour.

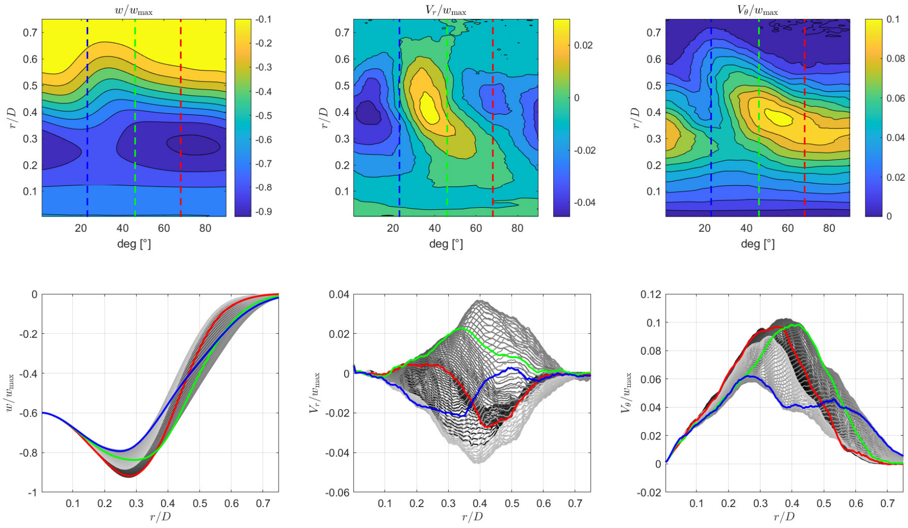

Figure 3.3: Mean quadrant: velocity fields and radial distributions - Passive swirl generator $S_{\text{design}} = 0.1$ and $S_{\text{calculated}} = 0.1107$.

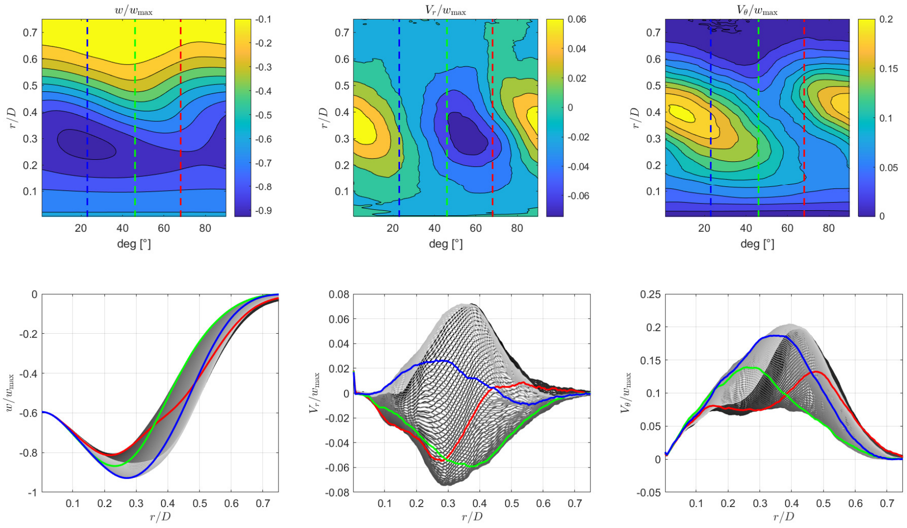

Figure 3.4: Mean quadrant: velocity fields and radial distributions - Passive swirl generator $S_{\text{design}} = 0.2$ and $S_{\text{calculated}} = 0.2059$.

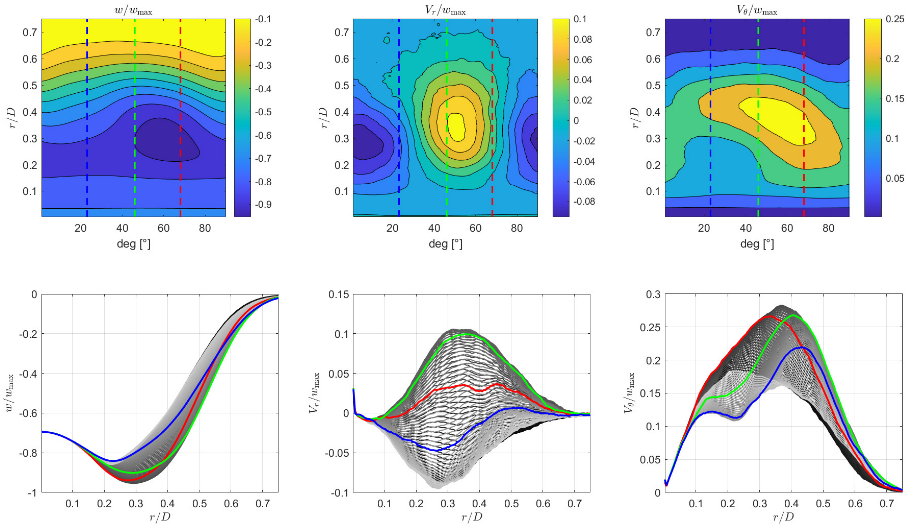

Figure 3.5: Mean quadrant: velocity fields and radial distributions - Passive swirl generator $S_{\text{design}} = 0.3$ and $S_{\text{calculated}} = 0.2858$.

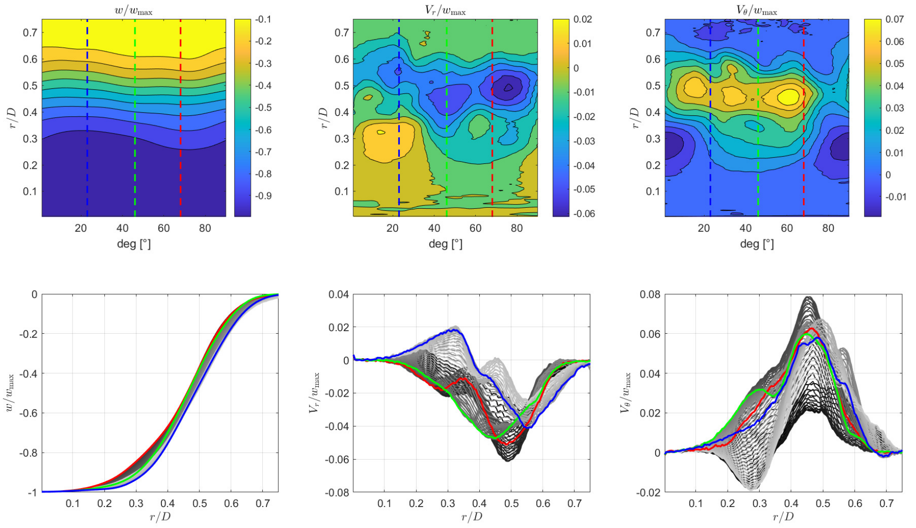

Figure 3.6: Mean quadrant: velocity fields and radial distributions - Passive swirl generator $V_{\text{pp}} = 10\ kV$ and $S_{\text{calculated}} = 0.0665$.

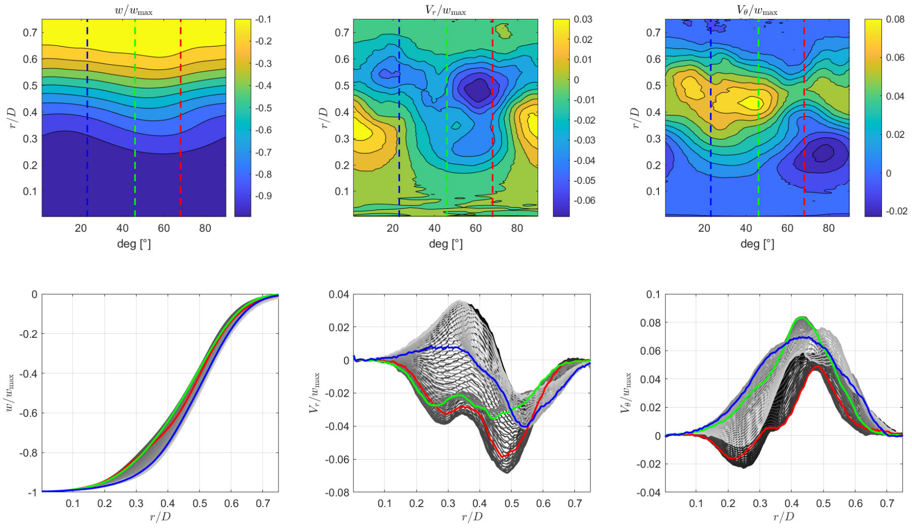

Figure 3.7: Mean quadrant: velocity fields and radial distributions - Passive swirl generator $V_{\text{pp}} = 12\ kV$ and $S_{\text{calculated}} = 0.0821$.

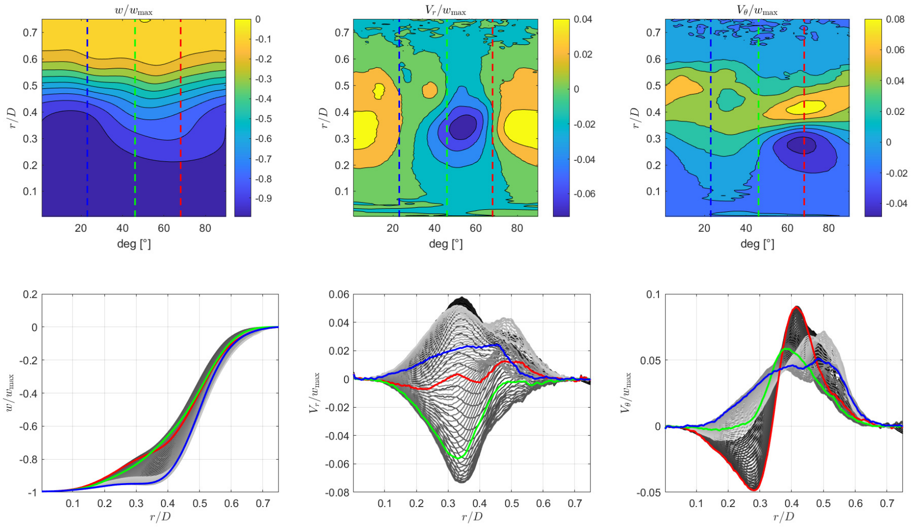

Figure 3.8: Mean quadrant: velocity fields and radial distributions - Passive swirl generator $V_{\text{pp}} = 14\ kV$ and $S_{\text{calculated}} = 0.0685$.

Radial velocity distributions

In terms of radial velocity distributions, it is essential to focus on the axial and tangential components as they play a significant role in the behaviour and dynamics of swirling jets.
With regard to the axial velocity component (see Figure 3.9), the axisymmetric jet exhibits its well-known top-hat radial profile, characterized by a constant velocity within the potential core. In contrast, swirling jets show distinctly different profiles. The jets produced by guided vanes (passive swirl generators) show a decrease in velocity near the jet axis ($r/D = 0$), with the peak occurring within the radial range of $0.2 < r/D < 0.3$ (see Figure 3.9). In the case of DBD-PAs (active swirl generators), however, the maximum axial velocity is observed at the jet axis, followed by a gradual decrease across the radial length. Furthermore, both methods exhibit a noticeable widening of the radial velocity distribution with respect to the axisymmetric jet, indicative of the expanding nature of swirling jets.

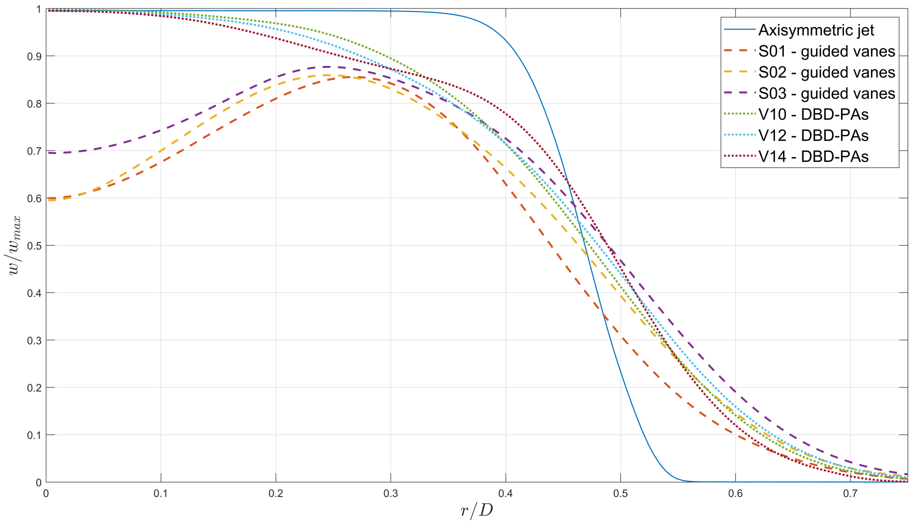

Figure 3.9: Radial distributions of the normalized axial velocity component.

Similarly, when examining the azimuthal component of the velocity vector (see Figure 3.10), distinct trends emerge between the two swirl generation methods, while for the axisymmetric jet, as per its nature, the tangential velocity remains zero. In the case of the guided vanes, the tangential component is present across almost the entire radial range and the maximum values shift to increasingly larger radial positions as the Swirl number increases. In contrast, for the active swirl generators, the azimuthal component does not extend up to the jet axis. The peaks, which are consistently lower than those measured for the passive swirl generators, are concentrated in the radial region (r/D), which spreads from 0.4 to 0.5 (see Figure 3.10). This corresponds to the position of the injectors' walls (i.e. where the electrodes were installed), suggesting that the DBD-PAs have only a localized effect on the flow.

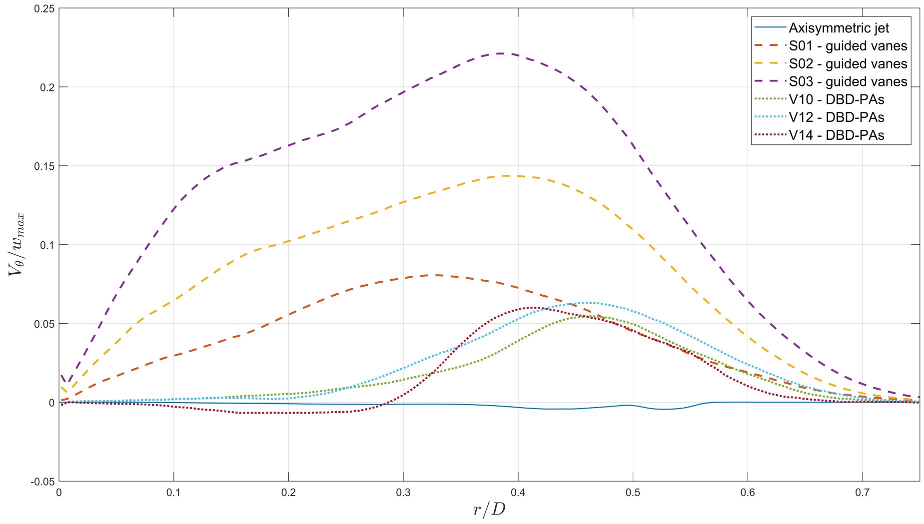

Figure 3.10: Radial distributions of the normalized tangential velocity component.

Circulation

Valuable insights can also be obtained from the radial distribution of the circulation (Γ), which is computed using the following expression:

$$\Gamma(r) = \oint_0^{2\pi} V_\theta(\theta, r) \cdot r \, d\theta \tag{3.2}$$

where $V_\theta(\theta, r)$ is the time-averaged tangential velocity, and r and θ are the radial and the azimuthal coordinates, respectively. The radial distribution shown in Figure 3.11 is obtained by evaluating the integral over all radial positions, with the circulation normalized by the quantity ($\pi w_{max} D$), where D is the injector diameter and w_{max} is the maximum axial velocity measured in each case.

As well as the radial distribution of the tangential velocity component, a clear difference can be observed in the circulation profiles between the active and passive swirl generation methods. In the case of swirling jets generated by DBD-PAs, the

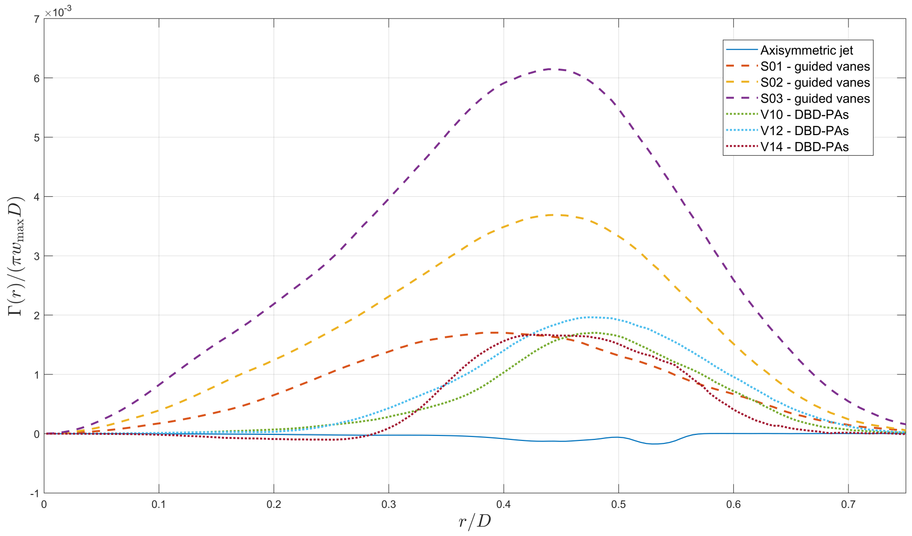

Figure 3.11: Radial distributions of the normalized circulation.

maximum circulation values are all located near the radial distance corresponding to the position of the electrodes ($r/D = 0.5$). In contrast, the circulation peaks for swirling jets generated using guided vanes tend to occur at smaller radial distances. Furthermore, as the swirl number increases, these circulation peaks move further away from the jet axis.

3.1.2 Vorticity

In light of the results obtained and the significant differences observed between the cases studied, the vorticity was calculated to provide another insight into the underlying phenomena that characterize the mean velocity fields. The equation used for its evaluation is the following:

$$\omega_z = \left(\frac{\partial v}{\partial x} - \frac{\partial u}{\partial y}\right) \tag{3.3}$$

where u and v are the horizontal and vertical components of the velocity vector, respectively.

Analysis of the vorticity fields shown in Figures 3.12 and 3.13 reveals distinct characteristics associated with passive and active vortex generation methods. In the former cases, it can be seen that the four lobes are less distinct and progressively overlap, eventually merging as the Swirl number increases. On the other hand, in the cases where DBD-PAs were employed, it is always possible to distinguish the four lobes, suggesting minimal interaction between them. Furthermore, by examining the velocity vectors, a significant difference emerges. In the passive cases - particularly for $S_{\text{design}} = 0.2$ and $S_{\text{design}} = 0.3$ - the swirling motion spreads from the jet axis to the wall region, indicating a more distributed swirling effect. In contrast, in the active cases, the velocity vectors are concentrated around the areas where the DBD-PAs are installed, with each lobe seemingly having its own swirling motion. This indicates that the effect of the plasma actuators is confined primarily to the wall region, and the limited interaction between the swirling regions results in more localized and isolated vortex structures.

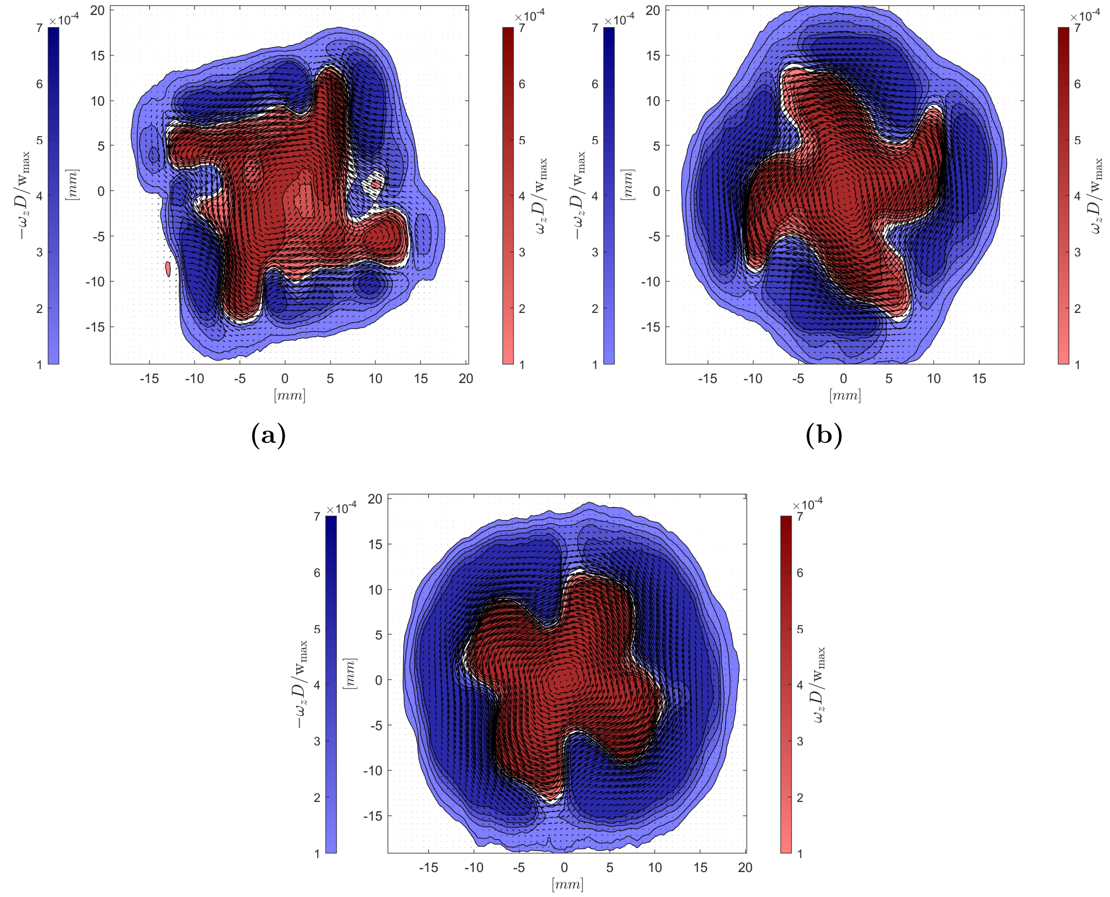

(a) **(b)**

(c)

Figure 3.12: Velocity vectors and normalized vorticity fields at $z/D = 0.5$ - Passive swirl generators: (a) $S_{\text{design}} = 0.1$, (b) $S_{\text{design}} = 0.2$, and (c) $S_{\text{design}} = 0.3$.

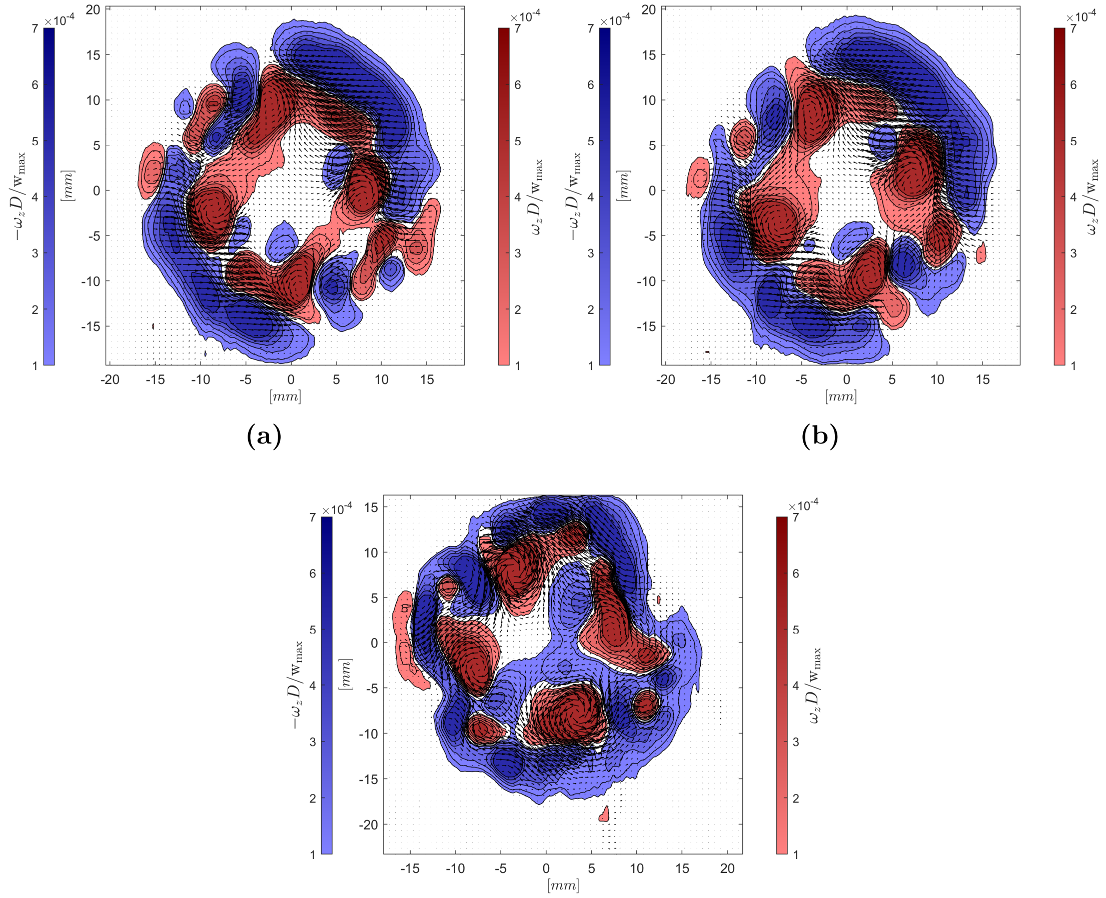

(a) **(b)**

(c)

Figure 3.13: Velocity vectors and normalized vorticity field at $z/D = 0.5$ - Active swirl generators: (a) $S_{\text{design}} = 0.1$, (b) $S_{\text{design}} = 0.2$, and (c) $S_{\text{design}} = 0.3$.

3.2 Three-dimensional time-averaged flow field

To reconstruct the evolution of the jets along their axis, S-PIV measurements were taken at several distances from the exit section. Specifically, eleven velocity fields were acquired from 0 *mm* to 125 *mm*, with each measurement spaced by half the injector diameter (12.5 *mm*). After post-processing each velocity field, a dedicated Matlab code was used to interpolate the data between the measurement planes and thus generate three-dimensional time-averaged flow fields.

3.2.1 Axial velocity

Figures 3.14 and 3.15 show the time-averaged axial velocity component of the flow field for the different configurations. The isosurfaces are set at $w/w_{max} = 0.5$, thus representing regions where the local axial velocity is half of the maximum value measured for each case. The cross-sections show the axial velocity contours and are positioned at various distances from the exit section in order to illustrate the velocity distribution as the jets evolve along the axial direction.

In accordance with the findings in [23], in the cases where passive swirl generators were used, it is noticeable - especially within a diameter distance from the exit section - that a non-homogeneous velocity distribution is induced along the azimuthal direction due to the presence of the guided vanes, which direct the flow in a helical pattern, reducing the axial velocity near the jet centre and increasing it near the edges. Furthermore, as the swirl number increases, a widening tendency can be observed and the jets emerging from the four vanes remain separated for longer distances. In fact, it can be seen that in the case corresponding to the lowest design swirl number $S_{\text{design}} = 0.1$, the separation between the four jets disappears rather quickly, so that the isosurface resembles that of the axisymmetric jet.

For the active swirl generators, on the other hand, the isosurfaces maintain a relatively constant shape and there doesn't seem to be any appreciable widening. Therefore, the jets emerging from the injectors equipped with DBD-PAs appear to have a similar behaviour to the axisymmetric jet, further confirming the low swirl numbers previously calculated.

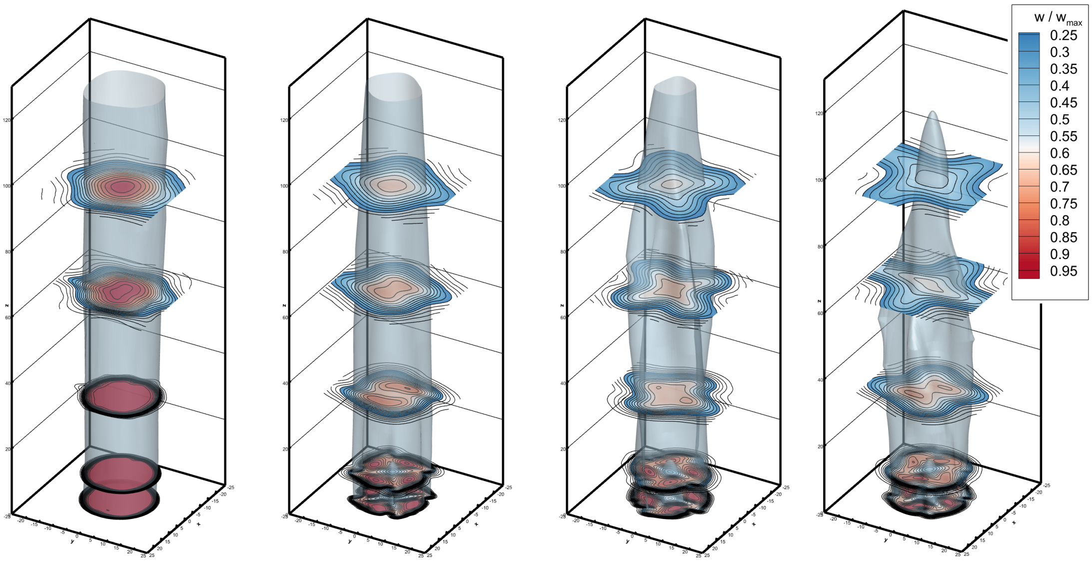

(a) **(b)** **(c)** **(d)**

Figure 3.14: Three-dimensional visualization of the time-averaged axial velocity component - (a) Axisymmetric jet and Passive swirl generators: (b) $S_{\text{design}} = 0.1$, (c) $S_{\text{design}} = 0.2$, and (d) $S_{\text{design}} = 0.3$.

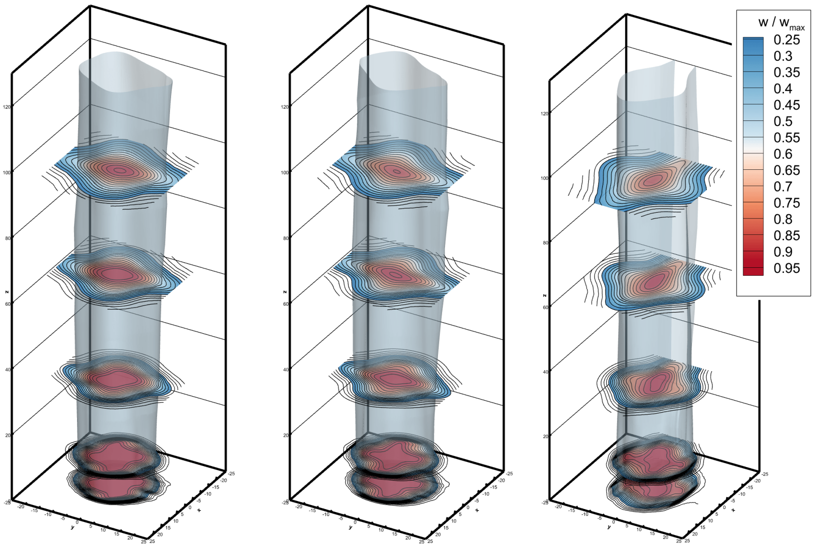

(a) **(b)** **(c)**

Figure 3.15: Three-dimensional visualization of the time-averaged axial velocity component - Active swirl generators: (a) $S_{\text{design}} = 0.1$, (b) $S_{\text{design}} = 0.2$, and (c) $S_{\text{design}} = 0.3$.

3.2.2 Tangential velocity

Evaluations obtained by assessing the axial velocity component of the flow field are supported by the analysis of the tangential velocity component.

It has already been pointed out in the section relating to Swirl number estimation that, when the passive swirl generators are used, the tangential velocity component results to be stronger and more widespread across the jet section precisely because of the effect of the guided vanes. This distinctive difference becomes even more apparent when looking at Figures 3.16 and 3.17, which show the isosurfaces set at $V_\theta / w_{max} = 0.09$ and the cross-sections representing the azimuthal velocity contours. Indeed, it is clearly visible that the isosurfaces of the passive cases, in addition to being larger and extending for longer distances from the exit section, tend to interact and entangle with each other as the Swirl number increases. Meanwhile, in the configuration where DBD-PAs are employed, the isosurfaces are confined near the region of the injector wall and almost completely disappear within two diameters from the exit section.

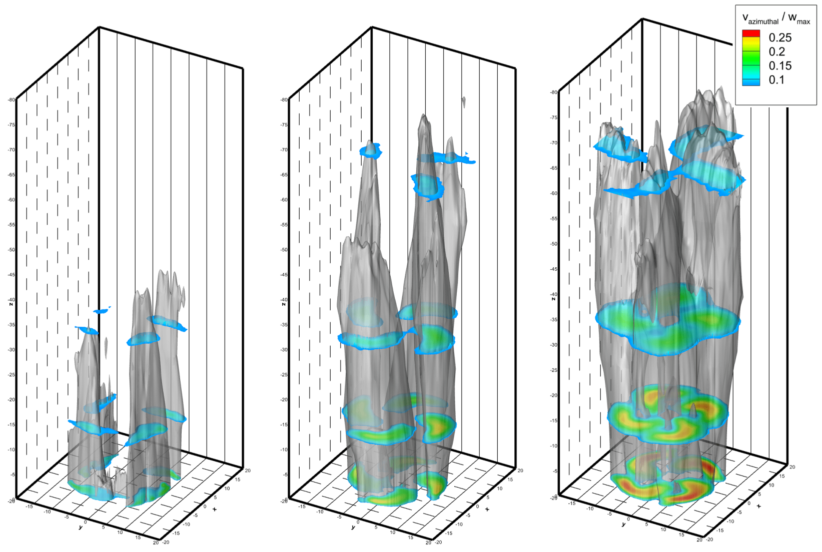

(a) **(b)** **(c)**

Figure 3.16: Three-dimensional visualization of the time-averaged tangential velocity component - Passive swirl generators: (a) $S_{\text{design}} = 0.1$, (b) $S_{\text{design}} = 0.2$, and (c) $S_{\text{design}} = 0.3$.

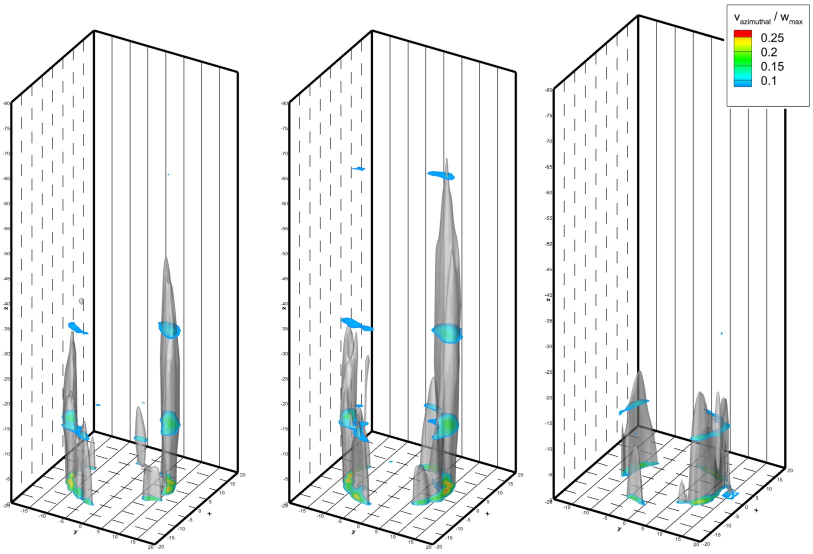

(a) **(b)** **(c)**

Figure 3.17: Three-dimensional visualization of the time-averaged tangential velocity component - Active swirl generators: (a) $S_{\text{design}} = 0.1$, (b) $S_{\text{design}} = 0.2$, and (c) $S_{\text{design}} = 0.3$.

3.2.3 Mass Flow Rate

Considering that one of the primary reasons for employing swirling jets is their enhanced entrainment compared to free jets, it is valuable to compare the mass flow rates for each configuration. This comparison serves as an additional benchmark to assess the performance of different swirl generation methods.

The mass flow rate ($\dot{m}$) was evaluated at each measurement section using a procedure similar to the one applied for calculating the circulation (Γ), but in this case, the integration was carried out over both the radial and azimuthal coordinates. The equation used to compute the mass flow rate is given by:

$$\dot{m} = \int_0^{2\pi} \int_0^R \rho \cdot w(r, \theta) \cdot r \, dr \tag{3.4}$$

where ρ is the density of the air, $w(r, \theta)$ is the axial velocity, and r and θ are the radial and azimuthal coordinates, respectively. Figure 3.18 shows the evolution of the normalized mass flow rate for each configuration, where the normalization has been carried out with respect to the mass flow rate at the exit section ($\dot{m}_0$). This approach was adopted because the jet facility is not equipped with a flow meter to ensure a uniform mass flow rate across all measurements. With the normalization, a direct comparison of the entrainment characteristics between different configurations is possible, despite the slight variations of the flow conditions.

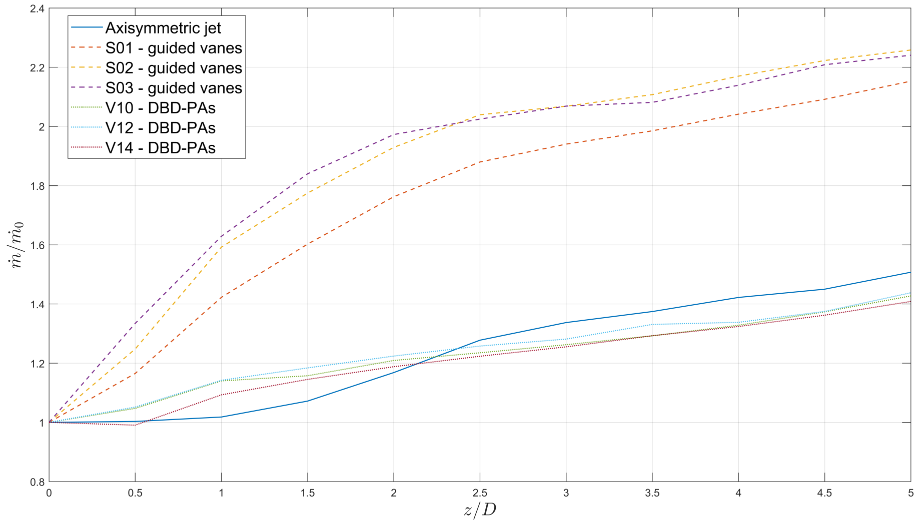

Figure 3.18: Evolution of the normalized mass flow rate along the jet axis.

This plot provides further confirmation of the previously drawn conclusions. In fact, the active and passive swirl generation methods exhibit distinctly different behaviors. For the guided vanes, the evolution of $\dot{m}/\dot{m}_0$ follows the pattern expected for a swirling jet, with an increase in mass flux as the distance from the exit section and the design Swirl number S_{design} increase, as a result of the enhanced entrainment. In contrast, the evolution of the active swirl generators mirrors that of the axisymmetric jet, with only a slight increase of the mass flux observed between 0.5 and 2 diameters from the exit section.

Chapter 4

Sequential triggering

In this chapter, the results obtained from the sequential triggering of the DBD-PAs are presented. The measurements were conducted under the same pressure drop conditions as those used in Chapter 3. Additionally, the same cylindrical polar coordinate system will be employed.

4.1 Phenomenology

To better appreciate the effects of sequentially triggering of the plasma actuators, a series of 20 S-PIV snapshots are shown in Figure 4.1, with each snapshot corresponding to a different phase in the sequence. These images capture the evolution of the flow over time as the plasma actuators are sequentially ignited.

It can be observed that the jet maintains a relatively stable and almost axisymmetric structure. However, sequential actuation leads to the generation of small, localized vortical structures which can be seen forming at the edge of the jet. These vortices gradually dissipate as the next actuator in the sequence is ignited. Despite the local perturbations, the overall impact on the center of the jet remains minimal. This limited influence of the plasma actuators is likely due to the relatively low voltage applied to the electrodes. In particular, the voltage used was the lowest applied during the simultaneous ignition measurement campaign ($V_{\text{pp}} = 10\ kV$). However, when only a single actuator is powered, higher voltages are required to achieve a significant effect on the flow. Unfortunately, this was not feasible due to the limited thermal resistance of the PLA material, which led to the melting of the injectors after a certain time and the subsequent interruption of the measurements. It should also be noted that although the voltage was set relatively low, the oscilloscope recorded peaks of 18 kV, probably due to interactions between the inhibited electrodes. This behaviour had a significant impact on the durability of the injectors.

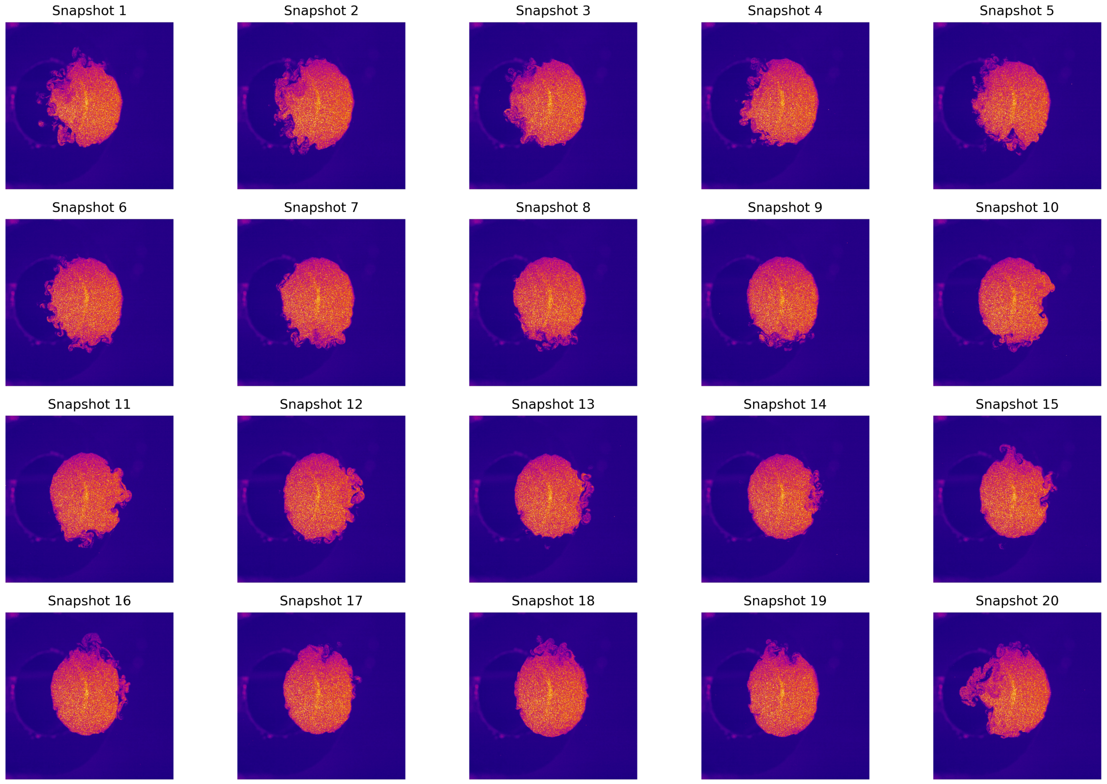

Figure 4.1: Sequential triggering: Evolution of flow structures over 20 phase-shifted snapshots.

4.2 Results

Given the above considerations, the results in this section are presented in a qualitative rather than quantitative manner. The primary objective is to demonstrate the functionality of this novel actuation method rather than to provide a detailed quantitative analysis.

Instead of focusing on the mean fields evaluated over all the acquired S-PIV snapshots, it is more appropriate to analyse the mean fields for each of the twenty sampled phases (Φ) individually. This approach highlights the behaviour of the flow when a single electrode is ignited and allows a more detailed investigation of the local effects induced.

Due to the large number of sampled phases, only a few are presented in this section to improve clarity and readability. The complete set of phase-averaged fields can be found in Appendix B for a more comprehensive overview.

4.2.1 Velocity

With regard of the velocity field, Figure 4.2 shows the axial velocity component with superimposed velocity vectors in the $x - y$ plane. It is particularly interesting to note that the sequential actuation of the DBD-PAs leads to the formation of localized regions in the proximity of the electrodes where the axial velocity is noticeably reduced, accompanied with the development of vortical structures. Furthermore, the direction of the velocity vectors appears to indicate the generation of a minimal tangential velocity component along the jet perimeter, although its overall influence on the flow is limited.

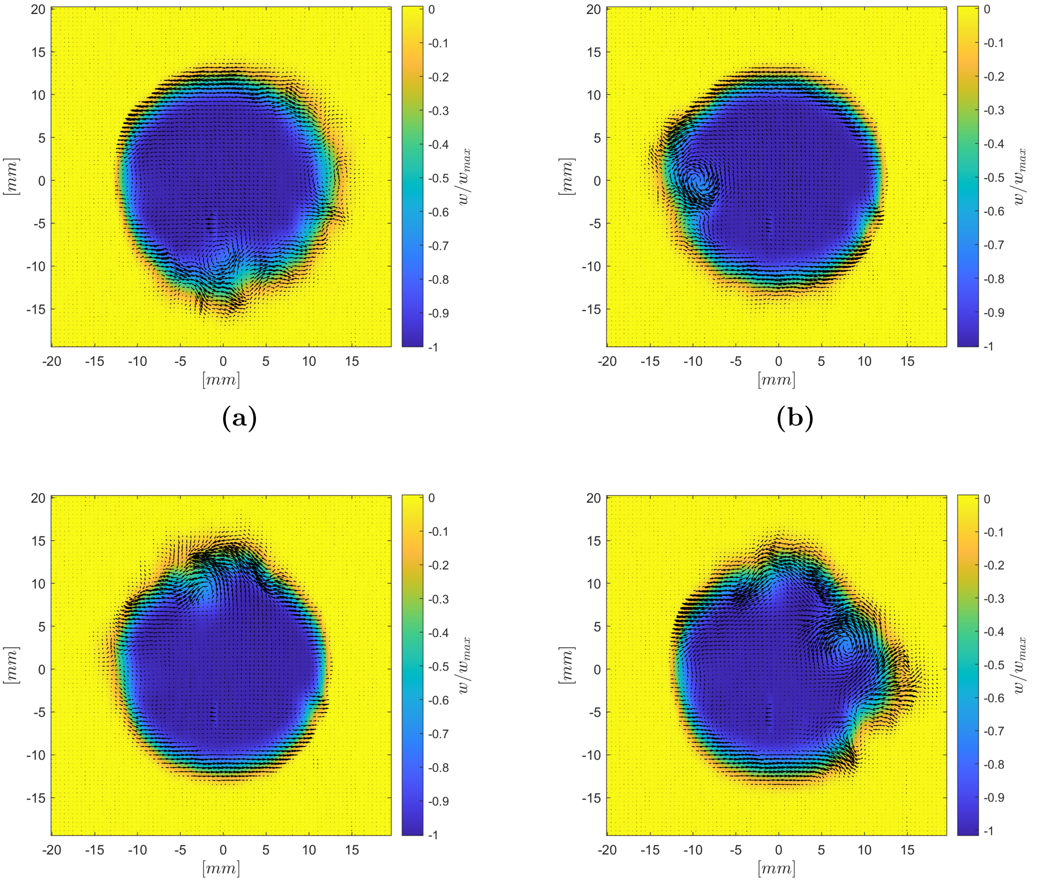

(a) **(b)**

(c) **(d)**

Figure 4.2: Sequential triggering - Velocity vectors and normalized axial velocity field at $z/D = 0.5$: (a) $\Phi = 90°$, (b) $\Phi = 216°$, (c) $\Phi = 288°$, and (d) $\Phi = 342°$.

4.3 Reynolds stresses

To gain a deeper insight into the turbulence characteristics introduced by this configuration, it is essential to examine the fluctuating behaviour of the flow. By using both the instantaneous and mean velocity fields, the fluctuating velocity components in the $x - y$ plane can be calculated as:

$$u' = u - \overline{u} \tag{4.1}$$

$$v' = v - \overline{v} \tag{4.2}$$

where $\overline{u}$ and $\overline{v}$ represent the ensemble-averaged velocity components, while u and v correspond to the instantaneous velocity components.

Following the calculation of the fluctuating velocity components, the Reynolds stress tensor components can be derived as follows:

$$\tau_{xx} = \rho\overline{u'u'} \tag{4.3}$$

$$\tau_{yy} = \rho\overline{v'v'} \tag{4.4}$$

$$\tau_{xy} = \rho\overline{u'v'} \tag{4.5}$$

The normal stresses are represented by τ_{xx} and τ_{yy}, while τ_{xy} represents the shear stress and provides information about the interaction between the two velocity components.

By averaging the instantaneous stresses for each phase Φ, the phase-averaged stresses can be obtained. Figure 4.3 shows the normalized phase-averaged shear stresses (τ_{xy}/w_{max}) of the selected phases.

By analyzing the distribution of Reynolds stresses (see Figure 4.3), it is evident that they are predominantly confined to the outer regions of the jet, with minimal impact on the core dynamics. This supports the speculation about the localized influence of the body forces generated by the DBD-PAs. In addition, it is noteworthy that the effect of the individual actuator vanishes after only a few phases.

4.4 Three-dimensional phase-averaged flow field

Another insightful visualization regarding the sequential triggering of the plasma actuators can be obtained by interpolating the phase-averaged quantities across a complete period. This approach results in the generation of a three-dimensional, phase-averaged flow field, which provides a clearer understanding of both the behaviour and influence of the DBD-PAs at each phase. In Figure 4.4, the translucent

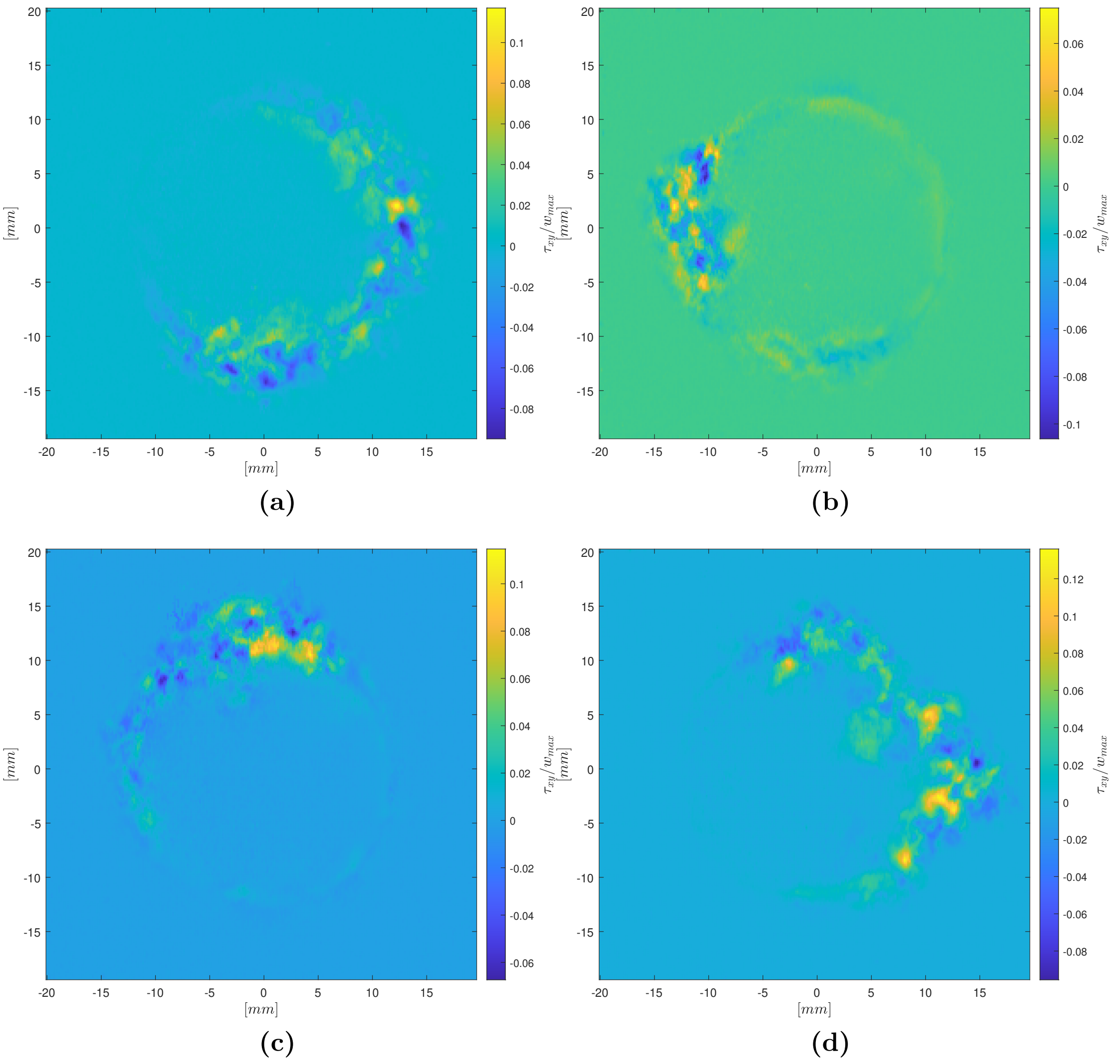

(a) **(b)** **(c)** **(d)**

Figure 4.3: Sequential triggering - Normalized phase-averaged Reynolds shear stress at $z/D = 0.5$: $\Phi = 90°$, (b) $\Phi = 216°$, (c) $\Phi = 288°$, and (d) $\Phi = 342°$.

isosurface represents the axial velocity component w, while the coloured isosurfaces illustrate the normalised Reynolds shear stresses (τ_{xy}/w_{max}). The cross-sections in the figure show the axial velocity contours and are positioned at significant phases in order to illustrate how the velocity distribution evolves as different electrodes are sequentially triggered. The isosurfaces of the Reynolds shear stresses highlight localized regions of elevated stress, which correspond to the perturbations introduced by the plasma actuators. These regions indicate where the actuators are actively influencing the flow. As the actuators are triggered sequentially, the flow field evolves and the stresses show how the jet responds to the induced perturbations at different phases.

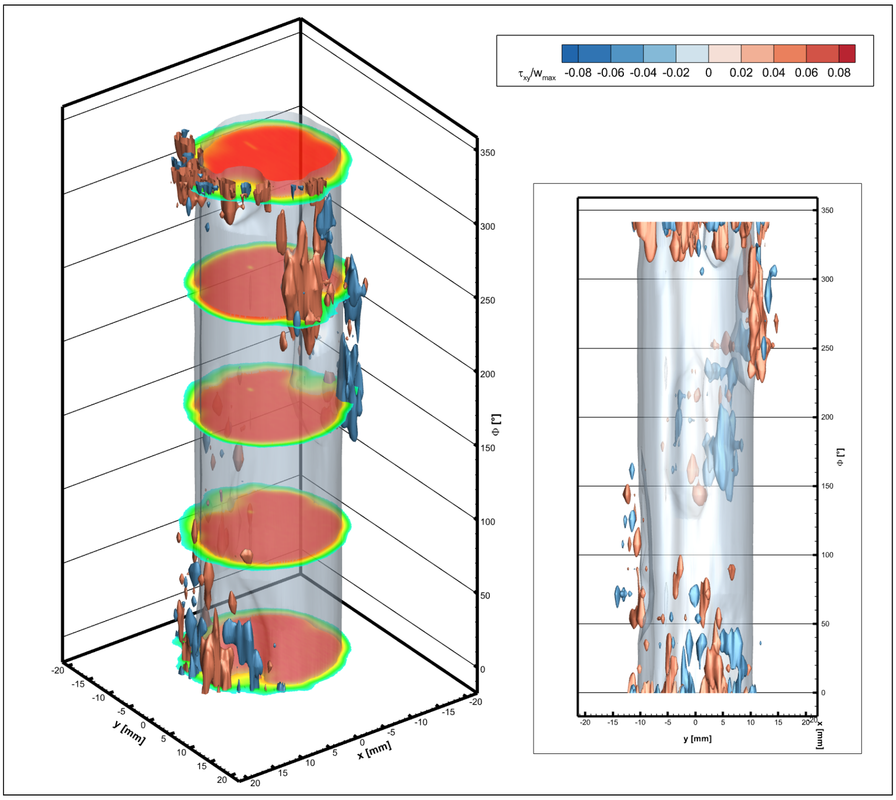

Figure 4.4: Sequential triggering: Three-dimensional phase-averaged flow field. Isosurface of axial velocity $w/w_{max} = 0.9$; isosurfaces of Reynolds shear stresses $\tau_{xy}/w_{max} = 0.43$ (red) and $\tau_{xy}/w_{max} = -0.43$ (blue).

Chapter 5

Conclusions

In this study, Stereoscopic PIV was used to investigate the feasibility of using DBD plasma actuators to induce an azimuthal velocity component into an axisymmetric jet, thereby generating a swirling jet.

The results consistently highlight the differences between active and passive swirl generation methods. While the passive method, in particular the guided vanes, successfully induces the expected swirling motion, the effect of the plasma actuators is limited to the perimeter of the jet and vanishes within two diameters from the exit section. Despite the limited influence, DBD-PAs appear to be a promising method for superimposing the tangential velocity component. In fact, the limitations of this work lie not in the concept itself, but in the dielectric material used, which does not allow to perform measurements at higher voltages.

Future measurement campaigns should be conducted using a different dielectric material, such as quartz. This would allow higher voltage differences to be applied between the electrodes, potentially improving the performance of the DBD plasma actuators and thus improving the induction of the swirling motion.

Appendix A

Round Jet - Symmetry Evaluation

Considering the novelty of 3D manufacturing and the fact that the jet facility was previously equipped with a completely smooth plexiglass nozzle, it was essential to verify whether the jets emerging from the 3D-printed nozzle could be considered axisymmetric before proceeding with the S-PIV measurements and Swirl number evaluation. To address this, a hot-wire measurement campaign was conducted for both the nozzle-only and nozzle and short pipe configurations.

A.1 Experimental Setup

The experimental setup used for this evaluation consisted of the jet facility (as described in Section 2.1), a hot-wire anemometer, and a linear stage system.

Hot-Wire Anemometer

The hot-wire anemometer system used for these measurements was the Dantec Dynamics StreamLine Pro, equipped with a P11 probe. Voltage signals were acquired using a NI-9215 DAQ module, and data were collected using a custom Matlab code. The acquisition parameters are summarized in Table A.1.

Frequency f [kHz]	**Acquisition time t [s]**
50	30

Table A.1: Acquisition parameters for the Hot-Wire measurement system.

The calibration of the system was made possible by using a previously derived correlation between the static pressure probes placed at the inlet and exit sections of the nozzle and a Pitot tube positioned in the jet's potential core. This correlation allowed the jet velocity at the exit section to be determined from the pressure drop across the nozzle alone, greatly simplifying the calibration of the hot-wire system. Specifically, the hot-wire probe was positioned near the exit section along the jet axis and measurements of both pressure (hence velocity) and voltage were acquired at varying pressure drops. The collected data were then fitted to a fourth order polynomial, providing the necessary coefficients to convert the voltage readings into velocity values.

A.1.1 Linear stage system

To ensure accurate movement of the probe and create a dense and reproducible measurement grid, a system composed of three linear stages was assembled. Specifically, two of the stages were motorized and used to move the probe across the x-y plane (parallel to the exit section), while the third stage, manually controlled, allowed for displacement along the z-axis. This setup enabled the evaluation of the jet's evolution at different distances from the exit section.
Two different measurement grids were defined: a simpler one to evaluate the radial distribution of the axial velocity and a more detailed one to assess the entire velocity field. In the former, the displacement between measurement points varied from 2 to 0.5 mm, while in the latter it varied from 5 to 1 mm.

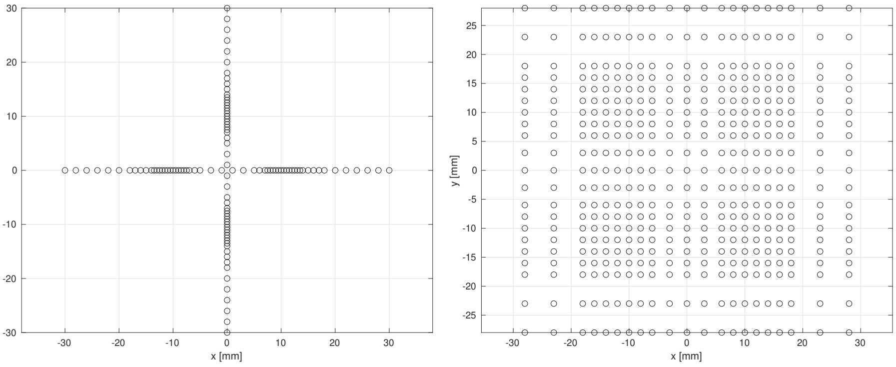

(a) **(b)**

Figure A.1: (a) Measurement points for the evaluation of the radial distribution of the axial velocity, and (b) Measurement grid for the evaluation of the velocity field.

It is worth noting that once the measurement grid was defined, a dedicated Matlab code handled the movement of the stages and the consequent acquisition of data from the hot-wire system.

A.2 Results

For both configuration the same set of measurement were carried out. The radial distribution of the axial velocity was evaluated at three different distances from the exit section, specifically at $z/D = 0$ and $z/D = 5$. The entire velocity field was measured at $z/D = 2$ and the Power Spectral Density (PSD) was evaluated at six key points within the field.

A.2.1 Nozzle Only

Radial distribution

Figures A.2 and A.3 present the normalized axial velocity and turbulence intensity profiles at the different measurement distances z/D. It is evident that the radial distributions remain symmetrical, even at significant distances from the exit section.

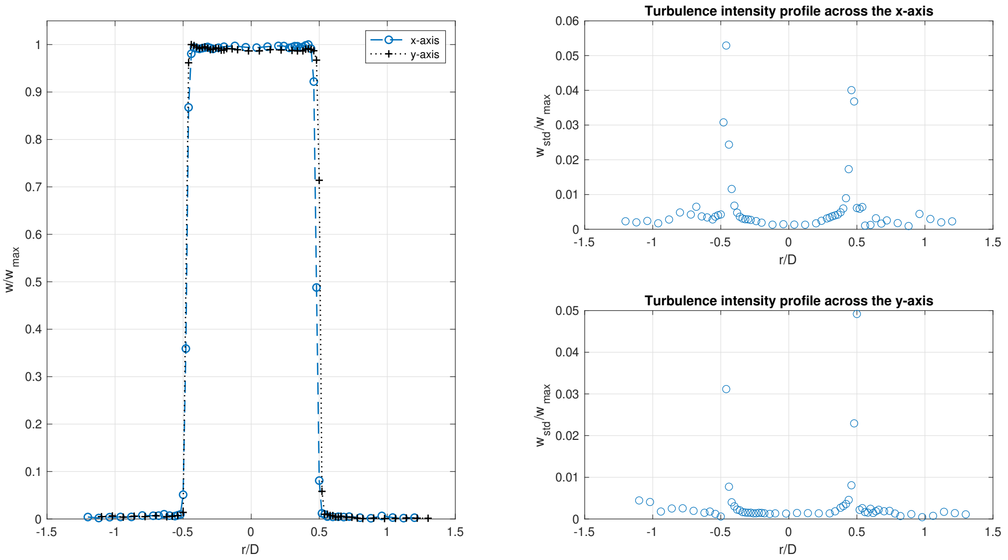

Figure A.2: Nozzle only - Radial distribution of the normalized axial velocity and turbulence intensity at $z/D = 0$.

Velocity field and PSD

Figure A.4 shows the velocity field acquired at $z/D = 2$ and it is possible to observe that the flow has a round shape, even though the spacing between the measurement points is considerable.

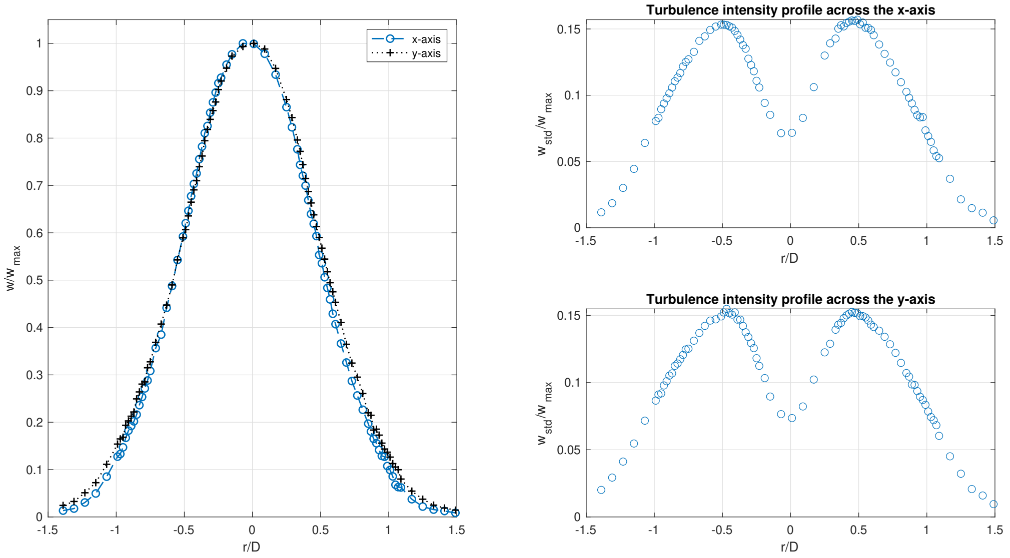

Figure A.3: Nozzle only - Radial distribution of the normalized axial velocity and turbulence intensity at $z/D = 5$.

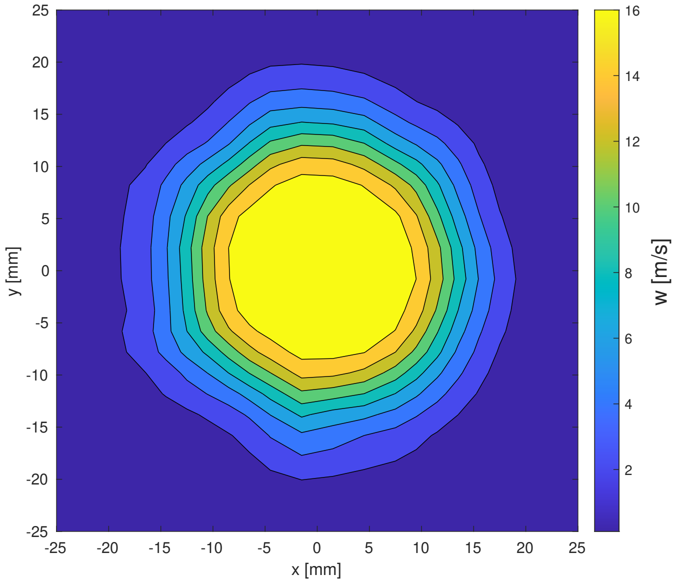

Figure A.4: Nozzle only - Velocity field at $z/D = 2$.

Figures A.5 and A.6 present the Power Spectral Density (PSD) evaluated along the $x - axis$ and $y - axis$, respectively, at three different measurement points. It is possible to observe higher frequency peaks as the radial distance from the jet axis increases. In fact, as confirmed from literature findings, the shear layer between the jet and the surrounding fluid is characterised by high velocity gradients, leading to instabilities and hence an increase in the frequency peak.

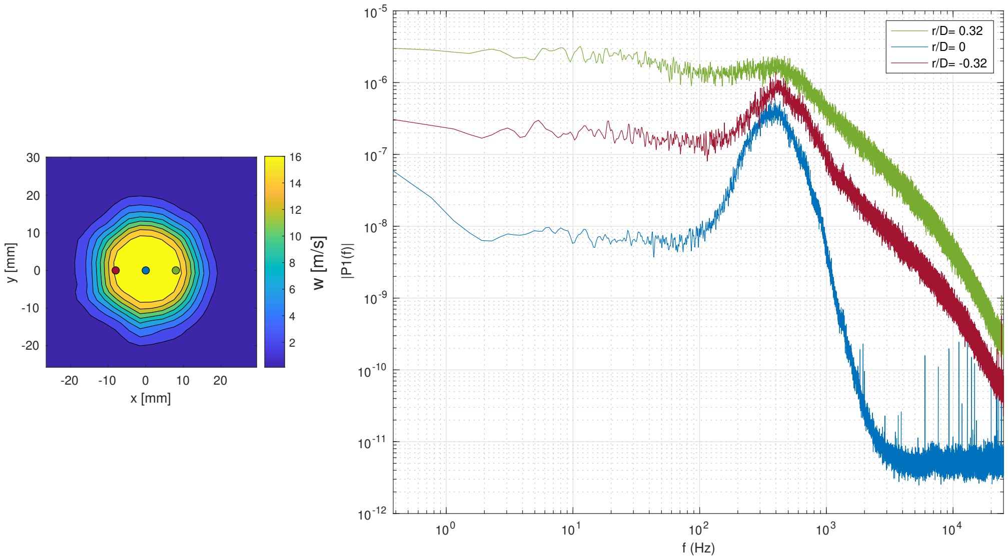

Figure A.5: Nozzle only - PSD across the y-axis.

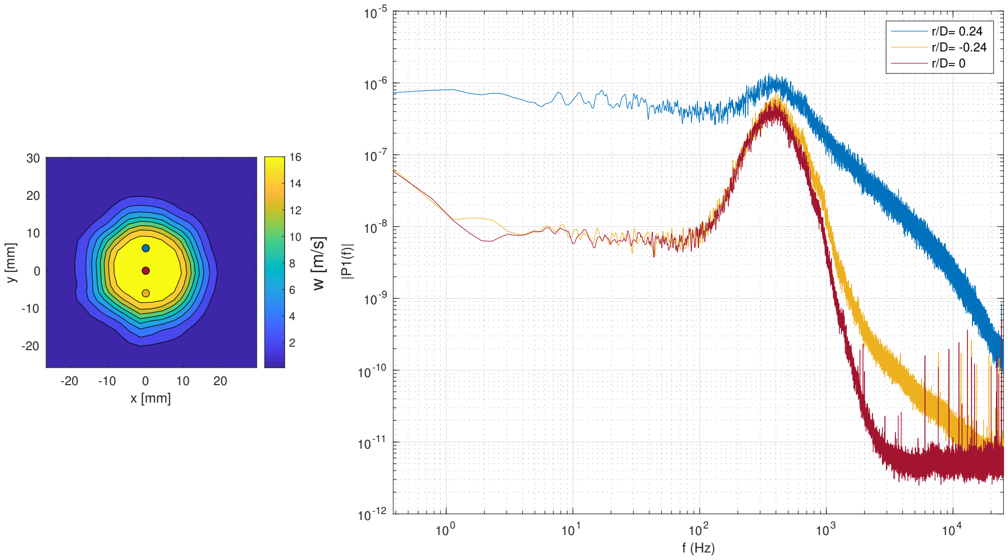

Figure A.6: Nozzle only - PSD across the z-axis.

A.2.2 Nozzle and Short Pipe

Here the results concerning the configuration of the jet facility with both the nozzle and the short pipe installed are briefly shown, as they show complete similarity to the configuration with the nozzle only.

Radial distribution

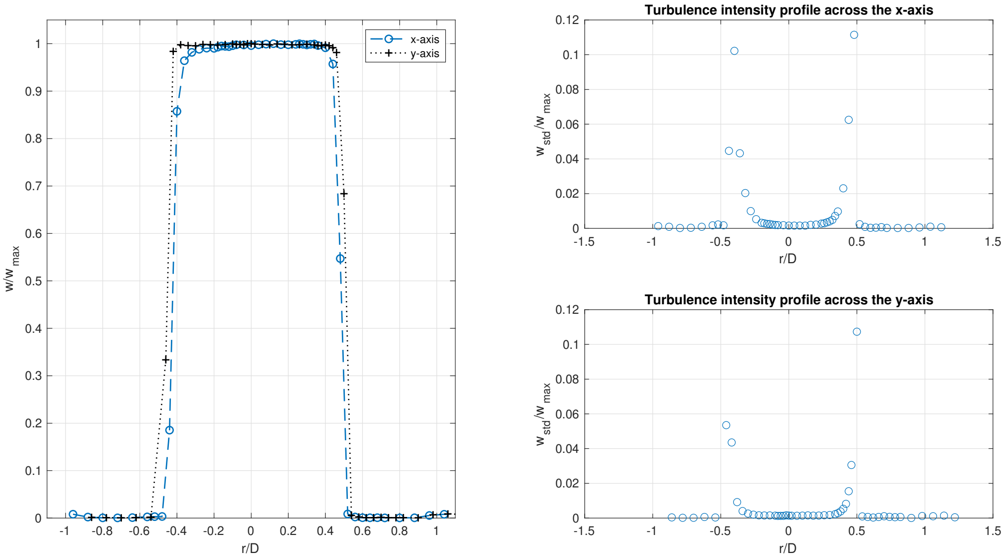

Figure A.7: Nozzle and Short Pipe - Radial distribution of the normalized axial velocity and turbulence intensity at $z/D = 0$.

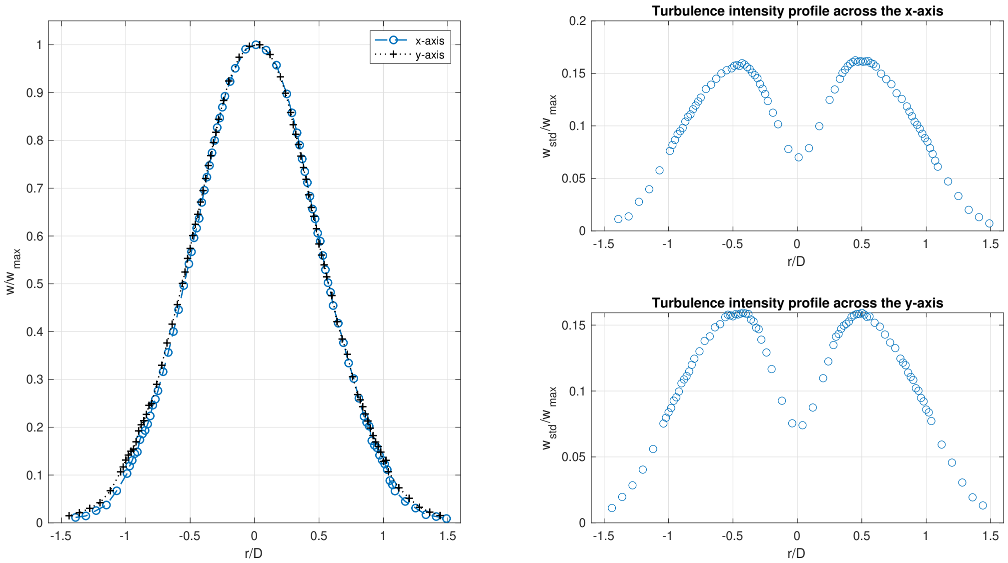

Figure A.8: Nozzle and Short Pipe - Radial distribution of the normalized axial velocity and turbulence intensity at $z/D = 5$.

Velocity field and PSD

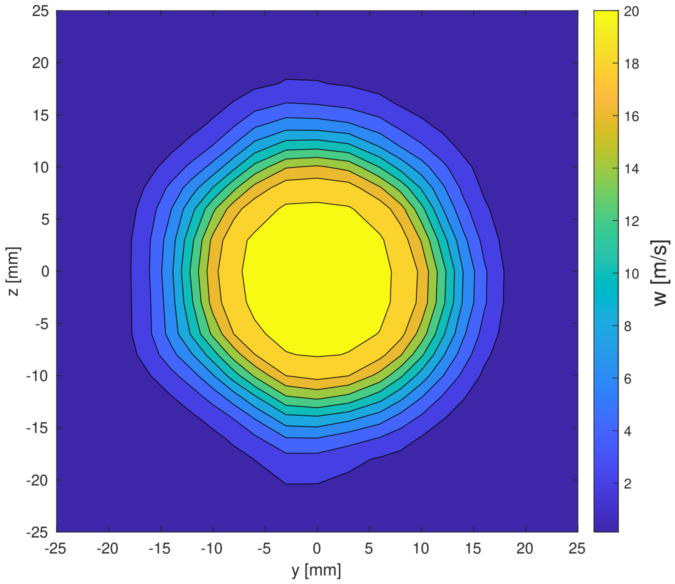

Figure A.9: Nozzle and Short Pipe - Velocity field at $z/D = 2$.

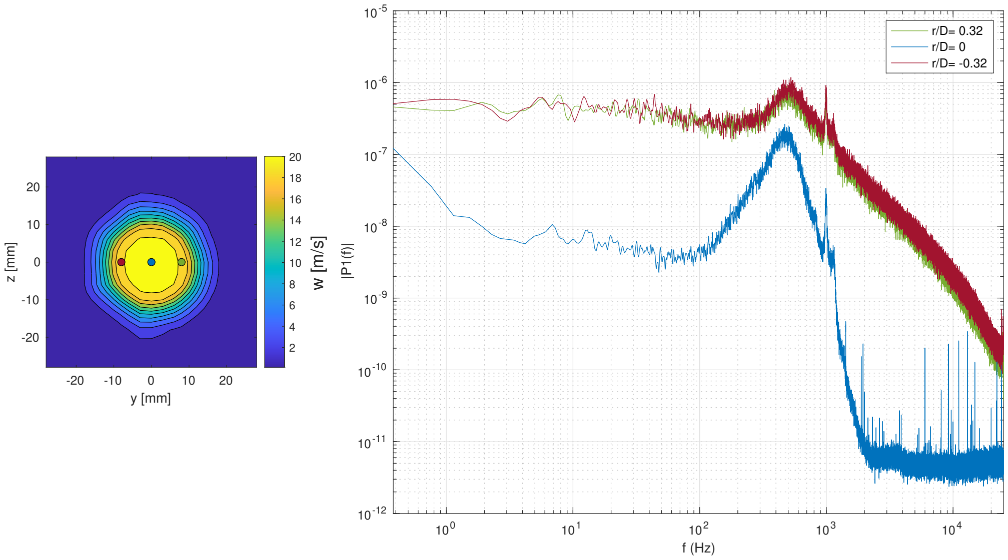

Figure A.10: Nozzle and Short Pipe - PSD across the y-axis.

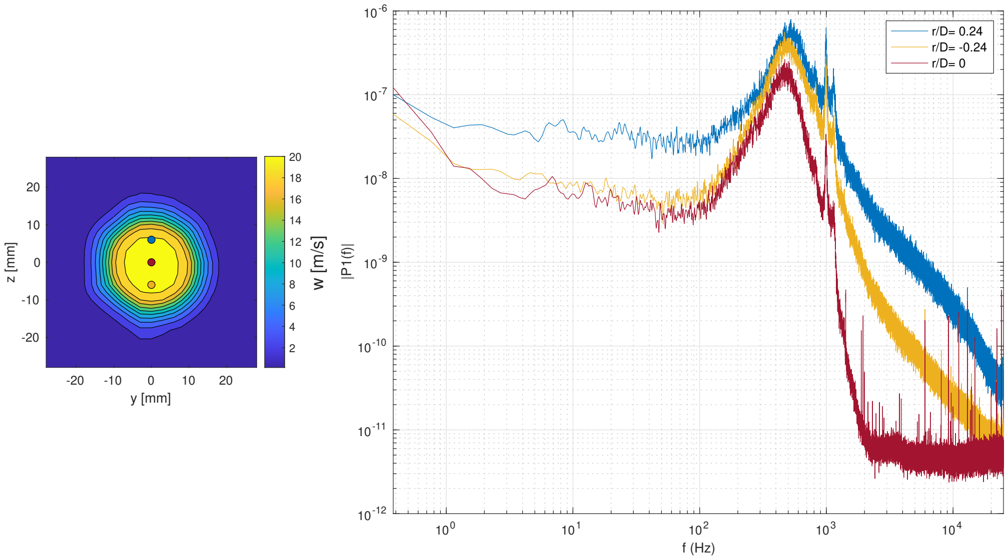

Figure A.11: Nozzle and Short Pipe - PSD across the z-axis.

Appendix B

Sequential triggering: phase-averaged fields

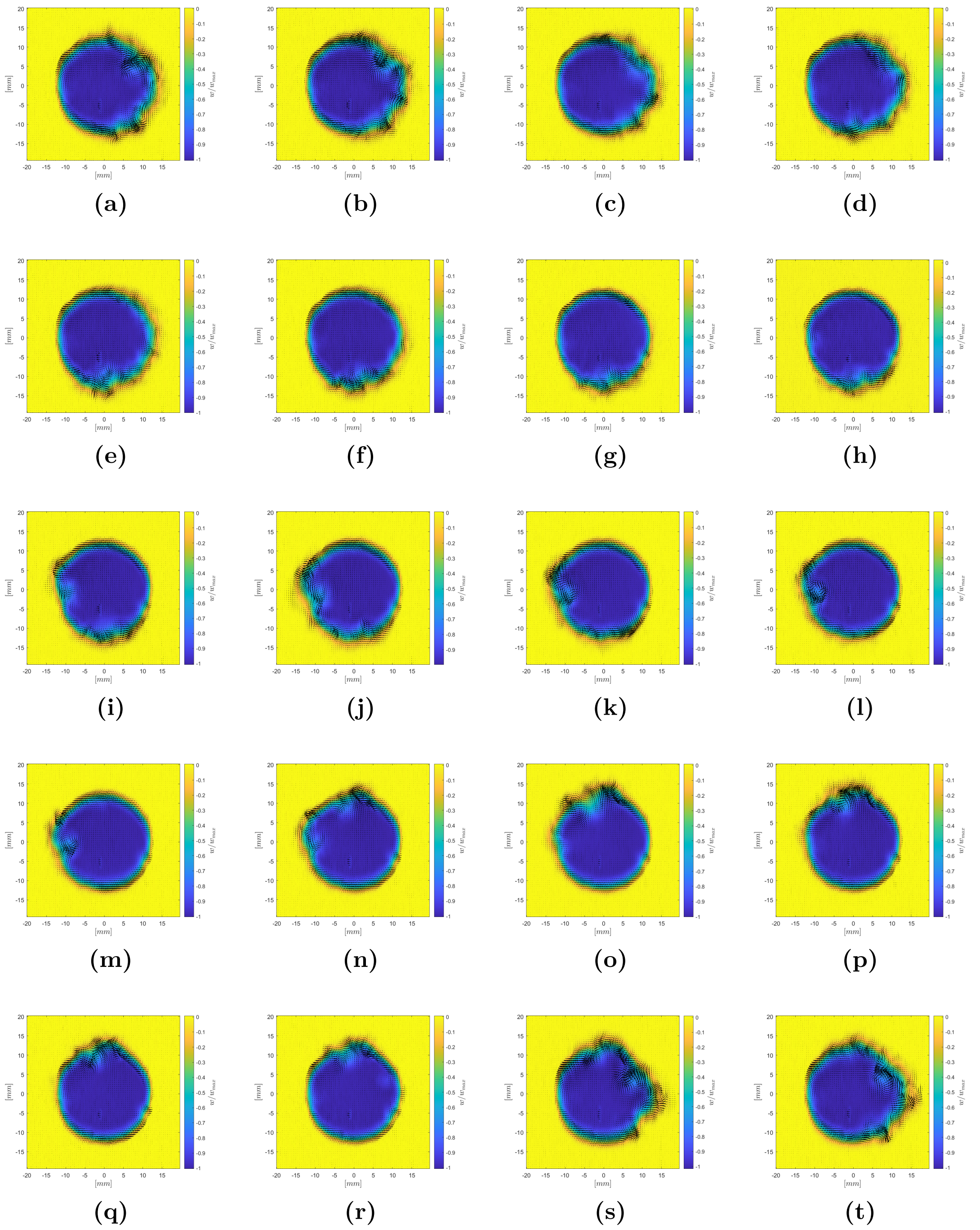

Figure B.1: Sequential triggering - Velocity vectors and normalized axial velocity field at $z/D = 0.5$. Complete set of phase-averaged fields.

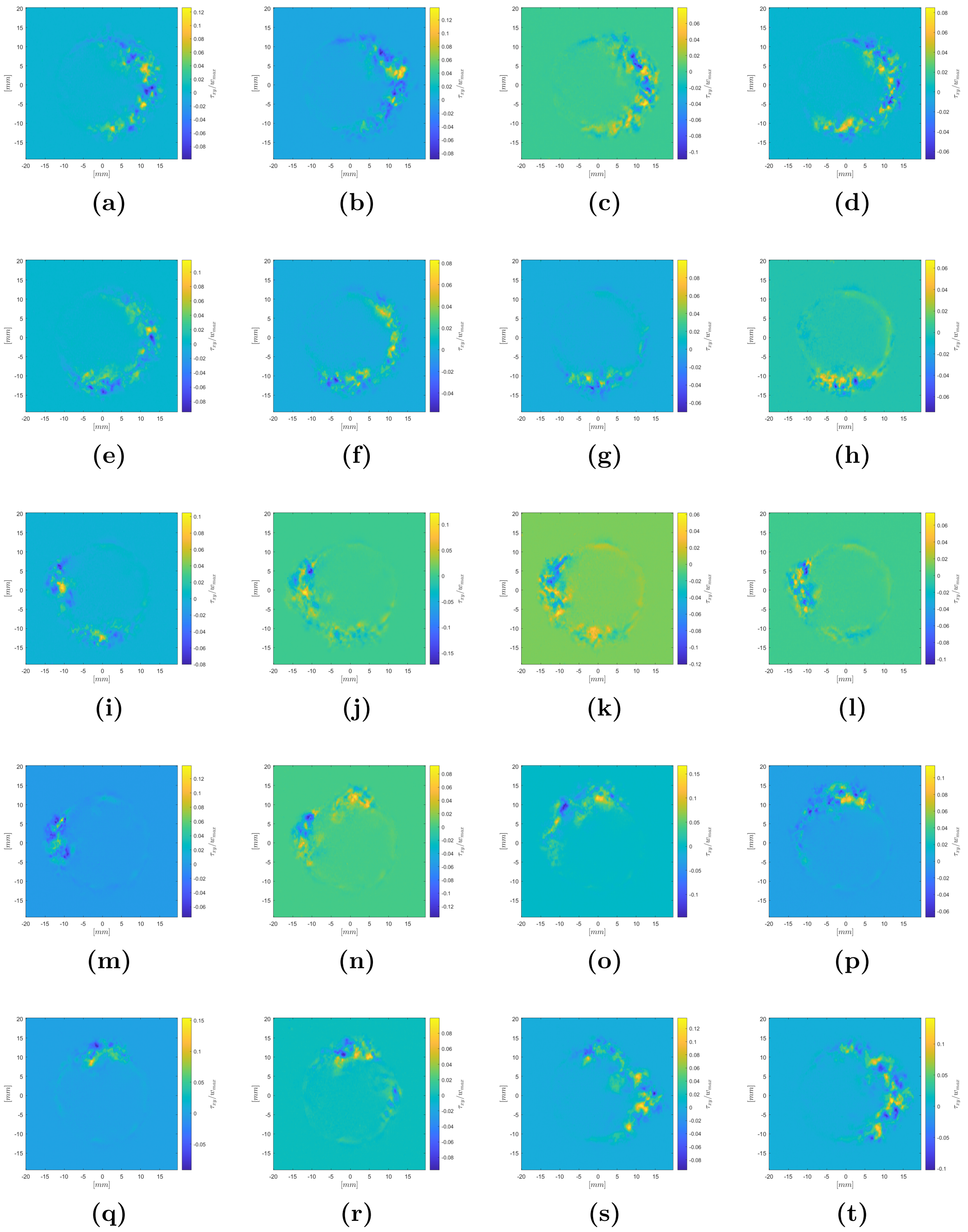

(a) **(b)** **(c)** **(d)**

(e) **(f)** **(g)** **(h)**

(i) **(j)** **(k)** **(l)**

(m) **(n)** **(o)** **(p)**

(q) **(r)** **(s)** **(t)**

Figure B.2: Sequential triggering - Normalized phase-averaged Reynolds shear stress at $z/D = 0.5$. Complete set of phase-averaged fields.

Bibliography

[1] Ing Kiet Toh, Damon Honnery, and Julio Soria. «Axial plus tangential entry swirling jet». eng. In: *Experiments in Fluids* 48.2 (2010), pp. 309–325. ISSN: 0723-4864 (cit. on pp. 1, 2, 7, 8).

[2] Norman Chigier and A. Chervinsky. «Experimental investigation of swirling vortex motion in jets». In: *Journal of Applied Mechanics* 34.2 (June 1967), pp. 443–451. DOI: `10.1115/1.3607703`. URL: `https://doi.org/10.1115/1.3607703` (cit. on pp. 1–5).

[3] Rahmat Taghavi and Saeed Farokhi. «Turbulent swirling jets with excitation». eng. In: *NASA CR-180895* (1988) (cit. on pp. 1, 7, 8).

[4] Paul Billant, Jean-Marc Chomaz, and Patrick Huerre. «Experimental study of vortex breakdown in swirling jets». eng. In: *Journal of fluid mechanics* 376 (1998), pp. 183–219. ISSN: 0022-1120 (cit. on pp. 2, 3).

[5] D. G. Lilley A. K. Gupta and N. Syred. «Swirl flows». In: *Abacus Press* (1984) (cit. on pp. 2, 28).

[6] Norman Chigier and J.M. Beèr. «Velocity and Static-Pressure distributions in swirling air jets issuing from annular and divergent nozzles». In: *Journal of Basic Engineering* 86.4 (Dec. 1964), pp. 788–796. DOI: `10.1115/1.3655954`. URL: `https://doi.org/10.1115/1.3655954` (cit. on pp. 2–4).

[7] J. P. Sislian and R.A. Cusworth. «Measurements of mean velocity and turbulent intensities in a free isothermal swirling jet». In: *AIAA Journal* 24.2 (Feb. 1986), pp. 303–309. DOI: `10.2514/3.9260`. URL: `https://doi.org/10.2514/3.9260` (cit. on p. 2).

[8] Andrea Ianiro and Gennaro Cardone. «Heat transfer rate and uniformity in multichannel swirling impinging jets». eng. In: *Applied thermal engineering* 49 (2012), pp. 89–98. ISSN: 1359-4311 (cit. on pp. 5, 7, 10, 15, 17, 29).

[9] Gang Li, Xi Jiang, Yujun Zhao, Cunxi Liu, Qi Chen, Gang Xu, and Fuqiang Liu. «Jet flow and premixed jet flame control by plasma swirler». eng. In: *Physics letters. A* 381.13 (2017), pp. 1158–1162. ISSN: 0375-9601 (cit. on pp. 6, 14–16, 30, 35).

[10] Gang Li and Xi Jiang. «Effects of electrical parameters on the performance of a plasma swirler». eng. In: *Physica scripta* 94.9 (2019), pp. 95601–. ISSN: 0031-8949 (cit. on pp. 6, 11–13, 16).

[11] Gang Li, Xi Jiang, Lei Jiang, Zhijun Lei, Junqiang Zhu, Yong Mu, and Gang Xu. «Design and experimental evaluation of a plasma swirler with helical shaped actuators». eng. In: *Sensors and actuators. A. Physical.* 315 (2020), pp. 112250–. ISSN: 0924-4247 (cit. on pp. 6–9, 13–15).

[12] Maarten Vanierschot and Guven Ogus. «Experimental investigation of the precessing vortex core in annular swirling jet flows in the transitional regime». eng. In: *Experimental thermal and fluid science* 106 (2019), pp. 148–158. ISSN: 0894-1777 (cit. on pp. 7, 9).

[13] Giovanni Maria Carlomagno and Gennaro Cardone. «Infrared thermography for convective heat transfer measurements». eng. In: *Experiments in fluids* 49.6 (2010), pp. 1187–1218. ISSN: 0723-4864 (cit. on p. 9).

[14] Jochen Kriegseis, Bernhard Simon, and Sven Grundmann. «Towards In-Flight Applications? A Review on Dielectric Barrier Discharge-Based Boundary-Layer Control». eng. In: *Applied mechanics reviews* 68.2 (2016). ISSN: 0003-6900 (cit. on p. 10).

[15] M Kotsonis, S Ghaemi, L Veldhuis, and F Scarano. «Measurement of the body force field of plasma actuators». eng. In: *Journal of physics. D, Applied physics* 44.4 (2011), pp. 045204–045204. ISSN: 0022-3727 (cit. on p. 11).

[16] Y. B. Suzen, P. G. Huang, J. D. Jacob, and D. E. Ashpis. «Numerical Simulations of Plasma Based Flow Control Applications». eng. In: Glenn Research Center, 2005 (cit. on p. 11).

[17] Simone Buselli. «Towards plasma-based swirling jets». MA thesis. Politecnico di Torino, 2024 (cit. on pp. 17, 28).

[18] John Levenhagen. «Converging Nozzle Design in an Anechoic Wind Tunnel». eng. In: *University of Florida* (2017) (cit. on p. 19).

[19] A. K PRASAD. «Stereoscopic particle image velocimetry». In: *Experiments in fluids* 29.2 (2000), pp. 103–116. ISSN: 0723-4864 (cit. on pp. 21, 22).

[20] K D Hinsch. «Three-dimensional particle velocimetry». eng. In: *Measurement science technology* 6.6 (1995), pp. 742–753. ISSN: 0957-0233 (cit. on p. 21).

[21] M. Raffel, Christian Willert, Steve Wereley, and Juergen Kompenhans. *Particle Image Velocimetry: A Practical Guide.* Jan. 2007. ISBN: 978-3-540-72307-3. DOI: `10.1007/978-3-540-72308-0` (cit. on pp. 22, 23).

[22] Carlo Salvatore Greco, Andrea Ianiro, Tommaso Astarita, and Gennaro Cardone. «On the near field of single and twin circular synthetic air jets». eng. In: *The International journal of heat and fluid flow* 44 (2013), pp. 41–52. ISSN: 0142-727X (cit. on p. 33).

[23] Andrea Ianiro, Kyle P. Lynch, Daniele Violato, Gennaro Cardone, and Fulvio Scarano. «Three-dimensional organization and dynamics of vortices in multichannel swirling jets». eng. In: *Journal of fluid mechanics* 843 (2018), pp. 180–210. ISSN: 0022-1120 (cit. on p. 47).